

**El Niño-La Niña events**

**simulated with Cane and Zebiak's model**

**and observed with satellite or *in situ* data. Part 1 : model data comparison**

by

Claire Perigaud and Boris Dewitte

submitted to J. of Climate

20 June, 1994

address:

Jet Propulsion Laboratory, MS 300/323, 4800 Oak Grove Drive, Pasadena. CA 91109-  
USA

## ABSTRACT

The Zebiak and Cane (1987) model is used in its "uncoupled mode", e.g. the oceanic model component is driven by FSU wind stress anomalies over 1980-1993 to simulate sea surface temperature anomalies and those are used in the atmospheric model component to generate wind anomalies. Simulations are compared with data derived from Geosat sea level, XBT temperature profiles, AVHRR SST, FSU winds and ISCCP cloud convection data.

Simulated variations of thermocline depth agree reasonably well with the sea level derived from Geosat or with the heat content in the upper 400m derived from XBT data. The model is fairly successful in reproducing the warm anomalies during El Niño events. But it fails to simulate the cold anomalies which are observed in AVHRR or in XBT data.

For both simulations and observations, the SST changes in the central Pacific are mostly determined by zonal advection. But the model simulates zonal current anomalies which are reversing at a 9-month frequency. Those oscillations correspond to a resonant mode of the basin. They can be suppressed by cancelling the wave reflection at the boundaries or they can be attenuated by increasing the friction in the ocean model. Projecting altimetric observations on Kelvin and Rossby waves provide an estimate for zonal current anomalies. Those reverse from eastward during El Niño to westward during La Niña events.

Forced by the simulated SST, the atmospheric model is fairly successful in reproducing the observed westerlies during El Niño events, although those are simulated not far enough to the west of the SST anomalies. But most of all, the model fails to simulate the easterlies during

La Niña 1988. The simulated forcing of the atmosphere is in very poor agreement with the heating derived from observed cloud convection data.

## 1. Introduction

Satellite observations provide a unique opportunity to analyze synoptic events such as El Niño La Niña oscillations. In addition, because those events are a manifestation of air-sea coupling, a combination of atmospheric and oceanic observations is needed. During the last decade, satellites were launched with a variety of instruments that do provide such synopticity and variety. In particular, Geosat altimetry provided sea level observations. Of course, the major limitation of studying El Niño events with Geosat comes from the short duration of the mission. Nevertheless it was possible to observe the strong event taking place over 1986-1988 with Geosat (Cheney and Miller, 1988). Satellite also provide data from which SST, wind vector, air-sea fluxes and convection heating can be derived. Today, except for wind vector, we can find data available during several consecutive years over the last decade. At the same time, a tremendous effort is undertaken during the WOCE and TOGA programs to gather as much *in situ* data as possible. In particular, XBT data provide subsurface oceanic information over several El Niño events.

Data are all the more useful as they are combined with models to try and simulate reality. Besides statistical models such as Barnett et al (1988), there are not many models based on dynamics of the coupled ocean-atmosphere system are available today. Very little has been done in terms of validation with observations. Cane et al (1986) were able to predict Niño

events with a simple coupled model. Today this model is currently used for predictions of El Niño events (see Climate Diagnostics Bulletins).

The Cane-Zebiak model (see Zebiak and Cane, 1987) is further referenced as CZ model. The code of the CZ model was kindly provided by Dr. Zebiak (LDEO), together with the wind forcing and the climatologic fields. The objective of our study is to better understand the interannual oscillations based on observations and simulations derived with the CZ model over the same period. In this study, we present results derived in the context of the uncoupled mode only, as explained in section 3. Results are presented in two parts. Part 1 consists in comparing simulations and observations in terms of sea level, oceanic currents, sea surface temperature and atmospheric wind anomalies. Part 2 consists in introducing observations in the model to examine the impact on the simulations.

Part 1 is organized as follows. In section 2, we describe the various data sets used in this study. In section 3, we give a brief description of the CZ model, describe the characteristics of our control run and examine the FSU wind forcing. We compare simulated and observed sea level in section 4, SST in section 5, oceanic current in section 6 and atmospheric wind in section 7.

## **2. Data sets**

### *2.1 Surface wind stress data*

Wind pseudo-stress anomalies from January 1964 to April 1993 were provided by Dr. Zebiak (LDEO). They have been calculated from the pseudo-stress product from Florida State University (FSU) as described in Goldenberg and O'Brien (1981). The data cover the model domain with a

resolution of  $2^\circ$  in longitude and latitude and one month in time. Those data correspond to the so-called "detrended version" processed as in Cane et al (1986) or in Zebiak (1993).

### 2.2 *Sea surface temperature data*

The sea surface temperature data come from AVHRR observations and were derived from the blended sea surface temperature analysis at National Meteorological Center (Reynolds, 1988). The data cover the model domain with a resolution of  $2^\circ$  in longitude and latitude and 1 month in time. The data cover January 1982 to August 1991. Anomalies were computed relative to the climatology over January 1985 to December 1988 and interpolated on the model grid.

### 2.3 *Sea level data*

Geosat sea level time series were provided by Dr Cheney (NOAA) from  $134^\circ\text{E}$  to  $90^\circ\text{W}$ ,  $30^\circ\text{S}$  to  $30^\circ\text{N}$ , from April 1 1985 to September 16 1989. This period covers the full duration of the mission, including the geodetic and the exact-repetitive mission. For a detailed description of the data sets, the reader is invited to refer to Cheney et al (1989). The orbit error has been reduced by removing a linear trend alongtrack between  $40^\circ\text{N}$  and  $40^\circ\text{S}$  in the central and eastern Pacific. In the western Pacific the removal was performed over extended arcs between  $60^\circ\text{S}$  and  $60^\circ\text{N}$  as in Cheney et al (1990). Compared to the data used in those two latter references, the Geosat data used in this paper are derived from an improved data set (Cheney et al, 1991), because they have been corrected with a more accurate orbit ephemeris and a more accurate tropospheric correction. The resolution is  $8^\circ$  in longitude,  $1^\circ$  in latitude and 1 day in

time. Those daily time series present gaps, especially after January 1989. It was checked that the poorest coverage (except for the month of October 1986) happened between June 19 1989 and August 5 1989 when up to 10% of ocean coverage can be missing. In order to get a continuous time series in space and time, the monthly average was first taken at each grid point and a spatial interpolation was done. The month of October 1986 had no data because the satellite moved into a 17-day repetitive orbit from September 28 1986 to November 7 1986. We computed the month of October as the average of the months of September and November 1986. Anomalies were then computed relative to the 4 year climatology from April 1985 to March 1989. Sea level anomalies are converted into thermocline anomalies, using a coefficient of proportionality equal to the density ratio of the ocean model ( $5.7 \times 10^{-3}$ ).

Authors are aware that those altimetric estimates may not have a very good accuracy. The Geosat series used in this paper still contain errors because the orbit error reduction process may have removed part of the large scale meridional oceanic signal (Miller, 1993). The space-time analysis we have applied is not optimal either. Today there is no full description in time, space and location available for the errors contained in Geosat. This is also one reason why the main objective of this paper is not a quantitative analysis of the model-data fit or misfit. We rather concentrate on a qualitative description and a tentative physical interpretation. Indeed the features described below using altimetric results have been double-checked with Geosat estimates that we have derived with totally different data processing techniques, in particular for the orbit error reduction process (see Chao et al, 1993). In addition, independant observations are provided with *in situ* data.

#### 2.4 *Vertical temperature profiles*

Global data sets of ocean temperature vertical profiles in the upper 400m were kindly provided by Doctor Warren White from SCRIPS. They provide bimonthly temperature data at 11 depths every 5° of longitude and 2° of latitude from (January-February) 1979 to (July-August) 1992. The XBT measurements were performed in the TOGA program and data were used to examine the upper ocean thermal structures (Tourre and White, 1994). Bimonthly climatology and anomalies were computed over this whole period. Over the tropical Pacific between 15°S and 15°N, the percentage of coverage is higher than 80% between 1980 and 1992, except west of 150°E and south of the equator. In order to fill in the gaps, we interpolated data from adjacent points in space. XBT data provide information about several quantities. They provide heat ocean content in the upper 400m which is intercompared in section 4 with the Geosat sea level variations and the simulated thermocline anomalies. According to the parameters of the model, the scaling factor to convert heat content into thermocline depth corresponds to  $1.5 \times 10^{21}$  Joule per unit of heat content. XBT data also provide sea surface temperatures which are intercompared in section 5 with the AVHRR data and the simulated SST. In addition, XBT data provide temperatures at a depth of 40m and 60m which are compared with the simulated entrainment temperature in Part 2.

#### 2.5 *Cloud convection*

Anomalies of cloud convection were kindly provided by Doctor Rong Fu from UCLA. Those anomalies had been derived from ISCCP C2 data covering July 1983 to December 1990 with a resolution of 2°5 in

longitude and latitude. They measure the monthly mean frequency of occurrence for cloud convection relative to the monthly climatology over the whole period. These anomalies have been used to examine the cloud thermostat regime (Fu et al, 1992). They have also been used to study the role of deep convection anomaly in El Niño events (Fu and Liu, 1993).

### 2.6 *Latent heat and solar radiation*

Global data sets of monthly anomalies of latent heat and solar radiation were kindly provided by Doctor Tim Liu from JPL. Those two ocean-air flux data-sets are presented in Liu et al (1993). The latent heat flux have been derived from SSMI data over July 1987 to June 1991 with a method developed in Liu (1988). The solar radiative flux have been computed over July 1983 to December 1990 from ISCCP data following the method presented in Bishop and Rossow (1991). Both fields have a resolution of  $2.5^\circ$  in longitude and latitude. There is no latent heat nor solar flux simulated in the standard configuration of the model. Those data are used in Part2 of this study.

### 2.7 *Climatology*

Note that one of the difficulties we have in this study is linked to the fact that our climatologic fields are not well defined because the periods covered by observations are not long. Because data do not cover always the same periods, they are relative to different climatologies. In addition, the model computes anomalies relative to some climatology which is also different from ours. Climatologies for wind, wind divergence, ocean currents, upwelling and SST correspond to the fields used in the standard run described in other papers (see e.g. Zebiak and Cane, 1987; Zebiak,

1993). Those fields were provided by Dr. Zebiak (LDEO) on a monthly basis on the model grid. Vertical temperature gradients at the surface and mean upper layer depth are assumed time-invariant and dependant on longitude only; those mean values are provided in the code. We have compared the SST climatology derived from AVHRR data over 1985-1989 only with the one derived over 1982-1992. The difference is less than 0.5°C. We have intercompared the thermocline climatologies in Geosat, in the XBT data sets and in the model. The difference can reach 5cm locally. This is another reason why it is not worthwhile to make an optimal estimation of the model-data misfit. The features described in this paper hold whatever the climatology. We have indeed examined the sensitivity of the model to the climatology of the thermocline depth (see Part2). We give some quantitative estimates because those come from statistics computed for spatially averaged quantities. The domains where data were averaged are defined by (\*) in the endnote. Those estimates are used only relatively to each other for comparing various data and various simulations over the same period.

### **3. Model and Control Run**

#### *3.1 General description*

The CZ model is that described in Zebiak and Cane (1987), with standard parameters. This model simulates anomalies relative to a seasonal climatology which is specified. In this paper, we only briefly describe the model. The reader can find the information on the physics and the equations of the model in Zebiak and Cane (1987). The detailed information needed to compare observations with simulations is given in the appendix. The model has three components. One is the baroclinic model

which determines the dynamic response of the ocean to wind-forcing, a second one is the surface layer model which computes the SST anomalies and a third one is the atmospheric model which simulates the wind response to SST anomalies.

### 3.2 *Uncoupled and Coupled mode*

The model can be run in a coupled or uncoupled mode. In the standard uncoupled mode, the baroclinic and surface layer models are forced by observed winds. This provides SST anomalies which are used to drive the atmosphere model. Thus, the only difference between running the CZ model in a coupled or uncoupled mode is that at each time-step, the wind used to drive the ocean is the observed one in the uncoupled mode whereas it is the simulated one in the coupled mode. For both modes, the choice of initial conditions is quite important.

In addition, the model outputs contain variables simulated by the atmospheric model, by the surface layer model and by the baroclinic model. In order to be consistent with the time-stepping scheme of the model, it was necessary to determine which variables among those are the prognostic ones. This is explained in the appendix.

### 3.3 *Control Run: Initial Conditions and FSU Forcing*

FSU wind stress anomalies are used to force the ocean model in the uncoupled mode. We started the model from rest in January 1964 and ran the uncoupled mode up to April 1993. Besides the spin-up, this run named "CR" for "control run", provides simulations which are used to initialize the coupled run in the standard case. It is the results from the CR between February 1980 and April 1993 which are examined in this paper.

FSU zonal wind-stress anomalies are presented along the equator between February 1980 and April 1993 in Figure 1. This period is characterized by three El Niño events, in 1982-1983, in 1986-1987 and in 1991-1993. Those events correspond to anomalous westerlies located in the central Pacific, mostly over NINO4(\*). Those three events have different characteristics. During El Niño 1982-1983, westerlies were the strongest and had the maximum extent to the east. During the first two El Niño events, westerlies were followed by easterlies, but during La Niña 1988, the easterlies were the strongest and had the largest extent to the east. The third El Niño event is the longest one. Up to April 1993, there were no easterlies yet. The westerlies in 1991 weakened in 1992, but strengthened again in early 1993. Because of those differences and the short period covered in this study, we do not compute a composite event nor decompose the signals into EOF. We rather concentrate on each event. Note that between events, observed winds propagate slowly to the east at about 15 cm/s. The tendency of winds to slowly migrate eastward has been noticed by Rasmusson and Carpenter (1982).

#### 4. Sea level

##### 4.1 *Simulated sea level*

Forced by this wind, the ocean model simulates all three El Niño events with strong sea level anomalies in the eastern and western equatorial Pacific (Figure 2a). Westerlies in the central Pacific generate a combination of downwelling Kelvin waves to the east and upwelling Rossby waves to the west. During La Niña in 1988, signals have opposite signs as the wind anomalies in the central Pacific are reversed. The positive and

negative anomalies have similar amplitude and duration for El Niño and La Niña events during 1986-1989. This is not the case for the first event. The thermocline in the eastern Pacific is shoaling for only 3 months in late 1983 whereas it is deeper than usual during 16 months in 1982-1983.

As found in Zebiak (1989), the 1982-1983 and the 1986-1987 events correspond to a cross-equatorial exchange of mass from south to north (Figure 2b). Also, those two events are characterized by oscillations in the  $5^{\circ}\text{S}$ - $5^{\circ}\text{N}$  band in phase with the oscillations in the  $5^{\circ}\text{S}$ - $15^{\circ}\text{S}$  band and out of phase in the  $5^{\circ}\text{N}$ - $15^{\circ}\text{N}$  band. It is quite striking that the scenario is very different for the third event. The cross-equatorial exchange is intense and takes place from north to south before the warm event, in fall 1991. There is a strong deficit of water generated by the wind at about  $10^{\circ}\text{N}$  in summer 1990.

Off equator, anomalies are characterized by westward propagation as evidenced along the sections  $5^{\circ}\text{S}$ - $15^{\circ}\text{S}$  and  $5^{\circ}\text{N}$ - $15^{\circ}\text{N}$  (Figure 2c and 2d). The westward propagation speed decreases with increasing latitude as Rossby waves and it is not found in the wind-curl. A large part of the simulated variance is explained by free Rossby waves. Before discussing this furthermore, let us now compare those simulations with observations.

#### *4.2 Comparison with sea level derived from GEOSAT*

Simulated sea level anomalies are first compared with altimetric variations from April 1985 to September 1989 along the equator (Figure 3a). The oscillations described above during El Niño LaNiña over 1986-1989 are observed in Geosat. The correlation with simulations is fair in the equatorial wave guide (see table 1a). The poorest correlation is 0.37 in

the central Pacific where the observed and simulated variances are weak. The altimetric variations zonally averaged are presented in Figure 3b. The 5°S-5°N and 5°N-10°N bands are actively involved in the meridional mass transport. We also find in this figure, some evidence of a transport from the equator to the north in 1986-1988 with oscillations in the 5°S-5°N band being out of phase of those in the 5°N-15°N band. Both of those results have been found in Miller and Cheney (1990) and agree with the model.

Let us now concentrate on the discrepancy between model and data. Firstly, observations indicate that there is much less variability than in the model poleward of 5°. Secondly there is no evidence of westward propagation along the zonal sections north or south of the equator (compare Figures 3cd with Figures 2cd). Thirdly, the maximum of observed variability in the equatorial wave guide is located at 160°W, which is about 20° west of the simulated one. Fourthly, the amplitude of the observed anomalies in the equatorial wave guide decreases from the Central Pacific to the Eastern boundary whereas the simulated one increases.

Although it is possible that Geosat data contain large scale errors due to tropospheric content or orbit error reduction process, these model-data discrepancies cannot be due to data error only. Similar results were found in Miller and Cheney (1990) using Geosat data corrected with a different tropospheric correction. We also found similar results with Geosat data after processing the satellite data with a totally different technique in orbit error reduction (see Chao et al; 1993). Moreover, results are confirmed by independent observations which are derived from XBT.

#### *4.3 Intercomparison with sea level derived from XBT*

In addition, as Geosat, the comparison with the XBT data indicate the same features of model-data misfit. The simulated variability off equator is much larger than the observed one. There is much less westward propagation along off-equatorial sections in the observations than in the model. In the equatorial wave guide, the distribution of sea level variability as a function of longitude is very different for observations and simulations (Figure 6). The observed maxima and minima are located to the west of the simulated ones by about  $10^\circ$  for the XBT and  $20^\circ$  for Geosat. East of the maxima, the observed variability is decaying whereas the simulated one is not. We checked that this is not due to tropospheric, tidal nor orbit errors in Geosat. The difference is quite large over a wide area ( $50^\circ$  of extension in longitude). This cannot either be due to contamination by land proximity. We also checked that this is not due to a lack of coverage in the XBT. As will be seen in section 6, the model simulates too much variability there because there is too much wave reflection at the boundary.

#### 4.4 Discussion

It is not surprising indeed that the complex reality cannot be represented by one baroclinic mode only. The first baroclinic mode corresponds to a thin upper layer (150m). It is suitable for the equatorial wave guide. With such a thin layer, it is not surprising that the variability simulated poleward of  $5^\circ$  is unrealistically large. In the rest of the paper, we concentrate on the equatorial wave guide only.

Even there, one baroclinic mode only cannot adequately represent the structure of the mean thermocline which is deeper in the west than in the east. Several authors have highlighted the importance of higher baroclinic modes in the Eastern Pacific (see e.g. Lukas et al, 1984; Kindle

and Phoebus, 1994) or that of a continuously stratified ocean (see e.g. McCreary, 1984).

In addition, the model contains too much remotely forced variance. We computed the Ekman pumping induced by the FSU winds. This provides the rate of changes of sea level which are locally forced:

$$\partial(h_e)/\partial t = - \text{curl} (\tau / \rho f)$$

As in Kessler (1990), we found that the locally driven changes along 5°N and along 5°S are well correlated with the observations. The agreement is not as good with simulations. This is because a large part of the simulated sea level variability is not due to local forcing, but to free wave propagation and boundary reflection. We will come back on this issue in section 6.

Nevertheless it must be kept in mind that the model is not the only source of model data misfit. The simulations are highly dependant on the wind which contains very large errors as well. An example of large wind error is given in the tropical Pacific in 1986-1988 by comparing FSU winds with ECMWF winds. Both more accurate sea level and wind observations with accurate estimates of data error are needed to further examine these questions. Given these uncertainties, the CZ model performs indeed fairly well in simulating interannual sea level oscillations in the equatorial wave guide. For long, wind-driven equatorial wave model have shown that they have a pretty good skill in simulating sea level (e.g. Moore and Philander, 1977; Busalacchi and O'Brien, 1981; Cane, 1984).

## 5. Sea surface temperature

### 5.1 Simulated SST

Simulated SST along the equator (Figure 7a) is characterized by warm anomalies over NINO3(\*) during the three El Niño events. As expected, the SST anomalies are linked to the thermocline anomalies in the eastern tropical Pacific. The link is weaker in the west because the mean thermocline is deep and the SST anomalies are small there. During El Niño events, downwelling Kelvin waves induce warm sea surface temperature in the central and eastern Pacific. It is striking however that the CZ model hardly ever simulates any cold event over this period. Let us compare with observations.

### 5.2 *Comparison with observed SST*

The observed sea surface temperature anomalies along the equator are presented in Figure 7b for AVHRR data and in Figure 7c for XBT data. The agreement between both data sets is fairly good (see table 2). The timing and location of the strong anomalies agree well. The variability observed with XBT is weaker than for AVHRR. This is probably due to the sparse coverage of the XBT as noticed above for sea level. Nevertheless the weakest variability of all is the one simulated by the model. During warm anomalies, the observed SST agrees well with the model. In particular during El Niño 1982-1983 event, a double warm peak, with the first one in December 1982 and the second one in July 1983, is observed as well as simulated. The reader should notice that the simulated warm events do not persist longer than observations as found in coupled runs (Zebiak, 1985). Indeed, the opposite happens for El Niño 1986-1987 simulated with the control run: the simulated warm event terminates in April 1987 when the observed SST reaches its maximum. The observed warm event terminates 9 months after the simulated one.

But the most striking result of this intercomparison is that the model fails to simulate the observed cold anomalies. In particular, La Niña in 1988 corresponds to a strong cold anomaly in the central and eastern Pacific in both data sets. It is simulated only very weakly in the easternmost Pacific. Local discrepancy between observations and simulations reach 2°C. Averaged over NINO3(\*), the simulated sea surface temperature is warmer by as much as 1.6 °C than the AVHRR value in November 1988. The reader can notice that observations indicate a general tendency for a fast eastward propagation during El Niño events (of the order of 290 cm/s), a fast westward propagation (of the order of 80 cm/s) during La Niña 1988. SST propagates to the east with the Kelvin wave speed when it is determined by thermocline displacements and it propagates to the west with the first baroclinic Rossby wave speed if it is determined by zonal advection. After the El Niño in 1982-1983 and before the El Niño 1986-1987, SST slowly propagates to the east at about 15 cm/s. This slow mode of propagation has been studied by several authors (e.g. Anderson and McCreary, 1985; Neelin, 1991; Chao and Philander, 1993). So observations in Figure 7b and 7c support that a combination of slow SST modes and fast ocean dynamic modes take place, as proposed in Jin and Neelin (1993) and Latif et al (1993). It is quite remarkable that over the same inter-event period, the FSU winds slowly migrate to the east as well (see Figure 1).

### 5.3 *SST and thermocline*

The link between SST and thermocline changes is examined for the model and the data over NINO3(\*) in Figure 8. According to Zebiak (1989), the oceanic heat content in the 5°S-5°N band increases over the 2

years preceding the warm event and rapidly decreases during the event. The warm event is expected to be terminated by the arrival in the eastern basin of the upwelling Kelvin wave via reflection of the upwelling Rossby waves at the western boundary. According to the delayed oscillator theory (see e.g. Schopf and Suarez, 1988; Battisti, 1988; Cane 1992; Graham and White, 1988), different processes (as vertical mixing and zonal advection) take time to transfer the information of the thermocline displacements to the surface and SST anomalies are expected to lag the sea level anomalies. The lead of the thermocline changes is not clear in our results. Miller and Cheney (1990) did not find either any build up prior to the 1986-1987 event. For all observations and simulations, the warming is rather simultaneous with the downwelling incoming Kelvin wave. The second warm peak coincides with the arrival of the downwelling Rossby wave reflected from the Kelvin wave at the eastern boundary. Unexpectedly, the weak simulated cooling in 1988 is even leading the thermocline anomaly. The observed displacements of the thermocline are not leading the observed SST changes.

#### 5.4 *SST and zonal advection*

We then concentrated on the central Pacific, where the model fails to simulate the cold anomaly in 1988. We found, as mentioned in (Zebiak, 1985; Battisti, 1988; Cane et al, 1990) that zonal advection plays the dominant role in the SST changes over the central Pacific. In the CZ model, the SST changes due to zonal advection are written as:

$$- \quad U_0 \quad \times \quad (T_{BAR} + T)_x \quad (1)$$

$$+ \quad U_{BAR} \quad \times \quad (T)_x \quad (2)$$

Term (1) corresponds to the advection by the anomalous surface zonal current  $U_0$  of the temperature (climatology  $T_{BAR}$  + anomaly  $T$ ). Term (2) corresponds to the advection by the climatologic zonal current  $U_{BAR}$  of the temperature anomaly  $T$ . Figure 9 shows that their sum fully explains the simulated SST changes. This figure also shows that the variations over 1985-1989 are not characterized by a Niño-Niña oscillation. We found that over 1980-1993, the simulated first term corresponding to the advection by anomalous zonal currents of mean temperature is not oscillating every 3 to 4 years as expected. It is oscillating more often at a higher frequency close to the annual one.

## 6. Zonal current

### 6.1 *Anomalous zonal current simulated in the CR*

The simulated anomalous currents in the surface layer (50m) are derived from the baroclinic currents in the upper layer (150m) and from the shear induced by the wind (see equations A8 and A9 in Zebiak and Cane, 1987). We first determined that it is the baroclinic current which contains the higher-frequency fluctuations. Along the equator (Figure 10a), the model simulates zonal current anomalies which do not present oscillations on the 3-4 year time scale, but reverse from eastward to westward almost every year. Indeed similar oscillations were found by Zebiak (personal communication). The frequency spectrum of the signal averaged over NINO4(\*) indicates a peak close to the 9-month period (Figure 11). This peak is not due to the wind forcing.

It corresponds to the resonance of the basin. With a 2.90m/s phase speed, Kelvin and Rossby equatorial waves take about 10 months to cross the entire Pacific back and forth (the Kelvin wave takes 2 months one way,

the Rossby wave takes 6 months via the first meridional mode and 10 months via the second meridional mode for the way back). Actually, second harmonic of this resonant mode (4.8 months) can also be seen in Figure 11. We can verify with the model that the 9-month oscillations are due to a resonant mode of the basin.

### 6.2 *Run O.BNDY0 and run O.FRIC*

We ran the model assuming various conditions at the meridional boundaries. The run where both the reflection of incident Kelvin waves at the eastern boundary and the reflection of incident Rossby waves at the western boundary are cancelled, is named run O.BNDY0. In this run, the velocity at the eastern boundary does not vanish, the amplitude of the Kelvin and the Rossby wave is determined from the wind only. In run O.BNDY0 (Figure 10b), the zonal current no longer reverses every 9 months. All the energy is concentrated in the low-frequency modes of the wind (Figure 11). The dominant frequency corresponds to the El Niño oscillations (close to 4 years). A second peak is found, which could correspond to the biennial oscillation. Note that run O.BNDY0 performs better than the CR in simulating the SST over NINO4(\*) (see table 2).

Indeed, the resonant mode is strong in the model because it has a weak friction. The model assumes a Rayleigh damping with a coefficient equal to 30 months. We then ran the model with boundary reflexions as in the CR but with an increased coefficient of friction. When the coefficient is equal to 9 months (run O.FRIC), the resonant mode is much weaker (Figure 10c) and there is relatively speaking, more energy at low-frequency than at 9 months (Figure 11). However, the amplitude of the current oscillations simulated in run O.FRIC is everywhere and always

much weaker than in the CR or in run O.BNDY0. This difference is particularly striking in the western Pacific. This needs to be examined with observed currents (see below). Let us first examine the sea level simulated in runs O.BNDY0 and O.FRIC.

The sea level also contains some energy at the resonant mode. This is the case for the sea level simulated in the CR, particularly in the western Pacific (see Figure 5b). To a lesser extent, this is also the case for the sea level derived from altimetry or from XBT. For the sea level, the energy at the resonant mode is relatively less important than at low frequency. This is because the sea level is a direct response to the low-frequency wind. Changing the boundary conditions or the friction does not affect the sea level as much as the zonal currents. Compared with observations, the correlation of the simulated sea level is slightly better than in the CR (see table 1b). The amplitude of the sea level anomalies simulated in run O.FRIC is smaller everywhere. In run O.BNDY0, it is smaller in the eastern and western Pacific along the equator. Off equator, it is smaller in the eastern Pacific. In the 5°-15° zonal bands, the sea level changes simulated in run O.BNDY0 are always smaller than 5 cm everywhere east of 160°W. This is closer to the observed changes (Figure 3cd and 4cd) than to the ones simulated in the CR (Figures 2cd). Indeed run O.FRIC and O.BNDY0 perform better in terms of explained variance than the CR (see table 1b).

With a similar model and over 1987-1988, duPenhoat et al (1992) have shown that the reflected Rossby wave in 1988 plays a role in reducing the locally driven one. Observations also show that there is some energy

reflected at the western boundaries (see Figure 5b and White et al, 1990). In addition, the role of the boundaries is fundamental for the ENSO oscillations (see e.g. Graham and White, 1990). Attenuating the reflexion at the boundaries or increasing the friction in the model as shown above does not fully account for what happens in reality. It is likely that higher baroclinic modes and nonlinearity also contribute to breakdown the resonant mode. This must be examined with more complex models. Let us rather compare the simulated current anomalies with observations.

### *6.3 Anomalous zonal current derived from GEOSAT*

Baroclinic current velocities can be derived from altimetry by projecting observed sea level on equatorial waves. Picaut et al (1990) showed that the zonal component could be derived from Geosat by applying equatorial geostrophy. This involves the computation of the second derivative of sea level in latitude. The projection on Hermite functions done below also involves a good resolution in latitude. This is doable with altimetric data because the satellite has a good spatial resolution, it may be hazardous to do so with XBT data because of the coarser resolution and gaps which those data present.

We projected Geosat sea level anomalies on Hermite functions and determined the Kelvin and the  $l=1$  to  $l=5$  Rossby modes of the first baroclinic mode assumed in the model. This mode has a latitudinal scale length of 356 km. The sea level variance observed between 5°S and 5°N by Geosat is then recovered by 95%. Averaged over NINO3(\*)-NINO34(\*)-NINO4(\*) or NINOW(\*) boxes, Geosat sea level anomalies and the anomalies reconstructed from their projection always differ by less than 1cm. Note that the gridding and filtering in time and space performed on

Geosat data prior to the decomposition in wave modes may have altered some useful information contained in the along-track data (Picaut, personal communication). We compared our decomposition with those obtained from Geosat by Delcroix et al (1991) in terms of thermocline anomalies and by Delcroix et al (1994) in terms of zonal current anomalies. Note that in these two studies, the anomalies are computed over 1987-1988 and 1987-1989 respectively. They contain the interannual and the seasonal signals whereas our processing has been applied to the anomaly only relative to the climatology derived from Geosat over 1985-1989. Given those differences, the agreement between both estimations looks quite good.

The Kelvin and Rossby components of the zonal flow anomalies derived from Geosat are presented along the equator in Figures 12. All those signals were compared with the CR, the run O.BNDY0 and the run O.FRIC. The correlation with observations is better for the run O.BNDY0 and O.FRIC than for the CR (see table 3). As in Figure 3a, the altimetric Kelvin component (Figure 12a) has a maximum located in the Central Pacific (NINO34<sup>(\*)</sup> region) and not in the eastern Pacific. This is in better agreement with run O.BNDY0. As in the run O.BNDY0 and the run O.FRIC, the altimetric Rossby component (Figure 12b) is dominated by low-frequency oscillations rather than by the resonant mode at 9 months. The total anomalous zonal flow along the equator (Figure 12c) shows as expected that currents are reversing from eastward during El Niño 1986-1987 to westward during La Niña 1988 and that there is a general tendency for westward propagation. The energy spectrum was computed over 1985-1989 for simulated and altimetric currents (Figure 13). Note that over this period, the resonant mode is relatively less distinct than over 1980-1993

(compare with Figure 11). Altimetric current anomalies are dominated by the interannual oscillations. They also contain some energy at higher frequencies, which confirms that observations also contain some remotely forced motions. One peak is close to 13 months (and is found in the CR as well over this period). The another one is close to 6 months. This could be an indication of a more complex mechanism, like the presence of higher baroclinic modes. With a velocity equal to 1.80 m/s for the second baroclinic mode, the traveling back and forth of a Kelvin and Rossby wave takes 5 months for the first meridional mode and 7 months for the second one. Also note in Figure 13 that the energy observed at 4.6 years in Geosat is smaller than the one simulated in the run O.BNDY0 and larger than the one simulated in run O.FRIC or in the CR. This is another indication that in the Control Run, there is too much energy going in the remote forcing and not enough in the local forcing. Those questions must be reexamined with more accurate data over a longer period and with a more sophisticated ocean model.

We then plotted the SST changes and the zonal terms of advection computed from observations only (Figure 14). As in simulations (see Figure 9), the SST changes are highly governed by the zonal advection over the NINO4(\*) region. In addition, Figure 14 shows that it is mostly the advection by anomalous currents which are determinant. In 1988, this term has a strong negative anomaly which was not present in the CR. We will examine in part 2 what is the impact of this term on the SST simulations.

## **7. Atmospheric wind**

### 7.1 *Observed and simulated wind*

The simulated zonal wind anomalies are presented along the equator in Figure 15. Remember that here the atmospheric model has been forced with the simulated SST anomalies described above, with all the errors that those anomalies contain. The CR succeeds in simulating the large-scale westerlies in the central Pacific during the three El Niño events. The striking result is that it never simulates easterlies. This is the major model data misfit found over this period (compare with Figure 1).

The link in time between SST and zonal wind is examined in Figures 16. The zonal wind anomalies averaged over NINO4(\*) are highly correlated with the SST anomalies averaged over NINO3(\*). As expected with a slave model, the correlation is almost equal to 1.00 for the simulations (Figure 16a). Observations indicate that the development of westerlies is simultaneous with warming but their weakening is leading the cooling (Figure 16b). In addition, the simulated wind is not displaced sufficiently far westward relative to the SST anomalies. Wind vector maps (not presented here) show unrealistically strong winds in the north-east (north of 10°N and east of 160°E) and in the south-west (south of 10°S and east of 160°E). This has been noticed by Zebiak (1985). But the model is also deficient in equatorial regions. Along the equator, the simulated variability of the zonal wind is very weak west of the dateline. During the three El Niño events, the simulated westerlies are located to the east of the observed ones (compare Figure 15 and Figure 1). Those results are illustrated by the statistics given in table 4a. The observed variability is weaker over NINO34(\*) than over NINO4 whereas this is not the case for

the simulated wind. Note that run O.BNDY0 simulates a wind in better agreement with observations than the CR.

The simulated meridional component agrees very poorly with the observed one (table 4b). The simulated meridional wind is much weaker than the observed one, north and south of the equator. The model performs also very poorly in simulating the wind stress curl. The major curl anomalies are located to the east of the observed one. The offset is quite big. In the 3°N-9°N (Figure 17a), the simulated curl is maximum at 140°W, which is about 40° east of the observed maximum. A similarly large offset is found south of the equator in the 3°S-9°S band (Figure 17b). The model simulates a very weak variability in the southwestern Pacific along the SPCZ whereas this is where the observed variability is maximum.

### 7.2 *Forcing of the atmosphere*

In order to understand why the wind is so poorly simulated in the CR, we then looked at the forcing terms of the atmosphere. In the CZ model, the atmosphere is forced by two terms which can be written as:

$$Q_T = -\alpha \text{ SST} \exp\{ (T_{\text{BAR}}-30) / 16.7 \},$$

and

$$Q_C = +\beta \text{ CVGN},$$

where SST is the sea surface temperature anomaly, T<sub>BAR</sub> is the climatologic sea surface temperature,  $\alpha = 0.03 \text{ m}^2 \text{ s}^{-3} (\text{°C})^{-1}$  and  $\beta = 1.6 \times 10^4 \text{ m}^2 \text{ s}^{-2}$ . CVGN is a function of anomalous and climatologic wind convergence and is computed by the model based on an iterative process. The total forcing Q<sub>T</sub>+Q<sub>C</sub> is assumed to represent the internal forcing of the atmosphere due to cloud convection. The total forcing simulated in the Control Run is presented along the equator (Figure 18a). During the three

El Niño events, the negative anomalies in the central Pacific correspond to the atmosphere gaining heat. But it is quite striking that over the whole 13 years, the model hardly ever simulates heat loss in the atmosphere. In addition, the strongest forcing is located in the central and eastern Pacific and is highly correlated with the simulated SST anomalies.

We then plotted the forcing term which can be derived from the cloud convection data (Figure 18b), which means that we plotted :

$$Q_{\text{obs}} = -\gamma \text{ CVCN},$$

where CVCN is the observed frequency of cloud convection. According to the model parameters (see the Appendix in Zebiak, 1985), the scaling factor to apply is  $\gamma = 5.3 \times 10^4 \text{ m}^2 \text{ s}^{-2}$ . Figure 18b shows that the forcing is then oscillating between El Niño periods with enhanced convection and La Niña periods with reduced convection. So during El Niño periods, the atmosphere is gaining heat, but during La Niña periods, it is losing heat. In addition, the strongest forcing is located in the western Pacific, between 150°E and 180° and not in the eastern Pacific. Also note that observed anomalies have a stronger amplitude than the simulated ones.

The simulated forcing is thus in very poor agreement with the observed forcing. So the deficiency of the model to correctly simulate the wind anomalies may not be due to missing physics in the atmospheric model. It can be due to inadequate simulated forcing. Indeed it is likely that the model is missing the forcing anomalies during La Niña periods because it is not simulating the cold SST anomalies. It is also likely that it is simulating a weaker amplitude because the simulated SST anomalies have a weaker amplitude than the observed ones. This will be examined in Part 2.

## 8. Summary

In this paper, a variety of *in situ* and satellite observations are used to validate a standard run of the CZ model over 1980-1993. This period covers three El-Niño events which are quite different. In particular, the El-Niño 1986-1987 was followed by a strong cold event La Niña in 1988. The model does simulate fairly well the alternance of downwelling and upwelling of the thermocline over the whole equatorial Pacific. It is successful in reproducing most of the warm events in the eastern Pacific. But it fails to reproduce the cooling event in 1988 in the central and eastern Pacific. It also fails to reproduce the strengthening of easterlies in the central Pacific during the cold events. The forcing term of the atmosphere is in very poor agreement with the heating observed from cloud convection data. In part 2 of this study, we further analyze this major failure, explain why this happens and how the model performance can be improved.

But improving the model performance in an uncoupled context does not warranty that the model predictability is improved in a coupled context because then, small errors in simulating the wind, the ocean dynamics and the SST get accumulated. So we have further examined the discrepancies between observations and simulations in the uncoupled mode. Those can be listed as follows. By comparison with observations:

- \* the simulated sea level variability poleward of  $5^\circ$  is overly large;
- \* the simulated sea level anomalies have a stronger amplitude in the NINO3(\*) area;
- \* the simulated sea level anomalies along the equator are located to the east of the observed ones by  $O(10^\circ)$ ;
- \* the simulated sea level anomalies along  $5^\circ\text{N}$  and  $5^\circ\text{S}$  are overly dominated by westward propagation;

- \* the simulated baroclinic zonal currents contain an overly prominent 9-month oscillation;

- \* the simulated warm SST anomalies have a weaker amplitude and do not last as long;

- \* the simulated wind anomalies are located not far enough to the west of the SST anomalies. The offset can be as large as  $40^\circ$  for the wind stress curl in the  $3^\circ\text{N}$ - $9^\circ\text{N}$  and  $3^\circ\text{S}$ - $9^\circ\text{S}$  band.

The first discrepancy is not surprising. A one and a half shallow-water model with 150m upper layer thickness is not likely to simulate reality far away from the equator. So we concentrated on oscillations in the equatorial wave guide.

The other deficiencies of the baroclinic model are due to the fact that the model simulates too much energy carried by free waves relative to the energy locally driven by the wind. The 9-month oscillations are due to the resonant mode of the ocean basin. They can be suppressed or reduced by allowing no reflection at the boundaries or by increasing the friction in the ocean dynamic model. It is likely that they would also be reduced by using higher baroclinic modes or more sophisticated models. Actually it is worth revisiting those questions with more accurate sea level data, more accurate wind data and more model experiments.

In the central Pacific, both the model and the observations confirm that zonal advection plays the dominant role in the SST changes associated with El Niño La Niña oscillations. This will be examined in Part 2 of this study.

**(\*) Endnote:**

Names with (\*) correspond to the following regions:

NINO3: (5°S-5°N, 90°W-150°W),

NINO34: (5°S-5°N, 120°W-180°),

NINO4: (5°N-5°S, 150°W-160°E),

NINOW: (135°E-152.5°E; 5°S-5°N),

NINO4N: (1°N-7°N, 150°W-160°E),

NINO34N: (1°N-7°N, 120°W-180°),

NINO4S: (1°S-7°S, 150°W-160°E),

NINO34S: (1°S-7°S, 120°W-180°).

## ACKNOWLEDGMENTS

Most of all, the authors thank Dr S. Zebiak (LDEO, Palisades) who provided the code and data files. They thank him for his assistance throughout the study since it started in December 1991. The authors also thank him and Dr. Mark Cane for fruitful discussions and comments about the manuscript. We thank Dr R. Cheney (NOAA, Rockville) who provided the 1985-1989 Geosat sea level time series. We thank Dr R. Fu (from UCLA, Los Angeles) for the cloud convection data. We thank Dr. W. White and Dr. S. Pazan (from SCRIPPS, La Jolla) for the XBT data. We thank Dr. T. Liu (from JPL, Pasadena) for the heat flux and solar radiative budgets. We thank PODAAC (from JPL, Pasadena) for giving us access to the AVHRR SST data. We thank Karim Dellal (student from ENSAE working at JPL) for computing support during 8 months in 1992.

The research described in this paper was carried out by the authors at the Jet Propulsion Laboratory, California Institute of Technology, under contract with the National Aeronautics and Space Administration.

## APPENDIX

### Information about the model which must be known to compare or combine simulations with data

This information is about the scaling, the spatial grid and the timing scheme consistent with the model. In order to introduce data in the model, it is also necessary to determine which variables among the ones used in the restart, are prognostic or diagnostic. Let us look at the different components of the model.

#### *A.1 The ocean baroclinic model*

The ocean model is a wind-driven equatorial wave model based on long-wave low-frequency approximation of Kelvin and Rossby wave decomposition for the first baroclinic mode. The dynamics and numerics of this model is described in (Cane and Patton, 1984). The parameters are the phase speed of 2.90m/s and an equivalent depth of 86cm. The drag coefficient used is  $3 \times 10^{-3}$ . The code is written in a rectangular basin extending from 124°E to 80°W and from 28.75°S to 28.75°N with a resolution of 2° in longitude and 0.5° in latitude. The variables updated at each time step (10 days) are the amplitude of the Kelvin wave, the non Kelvin sea level and the non Kelvin velocity components (let us call them Rossby outputs) inside the oceanic domain and at the boundaries.

#### *A.2 The ocean surface layer model*

A surface layer is embedded in the upper layer in order to determine the evolution of the sea surface temperature anomalies. This surface layer is 50m thick everywhere. The model computes the surface velocity current

from the shear between the frictional Ekman currents and the baroclinic currents in the upper layer. Three dimensional advection by the mean and anomalous currents govern the SST changes. The code is written in a rectangular domain extending from 101.25°E to 106.875°W in longitude, and from 29°S to 29°N in latitude with a resolution of 5.625° in longitude and 2° in latitude. The model is time-stepped every 10 days, with an iterative process to verify the CFL conditions. The model needs the baroclinic currents as inputs to compute the shear in the upper layer due to the frictional Ekman currents. It also needs the thermocline anomalies as input to compute the entrainment temperature vertically advected. So the Kelvin amplitude and the Rossby outputs of the baroclinic model are converted into thermocline depths and currents in the shallow-water model. The equivalence between the baroclinic model defined above and the shallow-water model used here corresponds to an upper layer thickness of 150m and a density ratio of  $5.7 \times 10^{-3}$ . The converted Kelvin and Rossby outputs are added and interpolated on the coarser grid of the surface layer model. Because the time-stepping of this model is done before the time-stepping of the baroclinic model, a restart of the whole ocean-atmosphere model contains both baroclinic and shallow-water variables, with the shallow-water variables on the coarse grid at time  $t$  and the baroclinic variables on the fine grid at time  $t+10$  days. As simulations are sensitive to initial conditions, much care was brought to introduce data in the ocean-atmosphere CZ model consistently with this configuration (see Part 2).

### *A.3 The atmospheric model*

The atmosphere is driven by a heating anomaly due to the sea surface temperature anomaly. The local heating  $QT$  is augmented by a term

QC introduced to simulate heating due to low-level moisture convergence anomaly. QT is proportional to the sea surface temperature anomaly. QC is a function of anomalous and climatologic wind convergence (Zebiak, 1985). The code is written on the same coarse grid as for the surface layer model. The wind convergence is used to compute the moisture forcing term QC of the atmosphere. So the solution for wind-convergence is determined by successive iterations from a first guess. If the value of SST over NINO3(\*) is smaller than  $0.1^{\circ}\text{C}$ , the first guess is zero. Otherwise, local heating, wind components and wind convergence are initialized with the values simulated at the previous time step. This is not meant to introduce a time-stepping in the atmospheric response. The objective is only to accelerate the convergence of the iterative process. Nevertheless, to be consistent with the model, local heating, wind velocity components and wind divergence are prognostic variables for the atmospheric model when the NINO3 SST index is larger than  $0.1^{\circ}\text{C}$ . When data are introduced in the model as in Part 2, much care was brought to do so consistently with the model.

**References**

- Anderson, D. L. T. and J. P. McCreary, 1985: Slowly propagating disturbances in a coupled ocean-atmosphere model. *J. Atmos. Sci.*, **42**, 615-629.
- Barnett, T., N. Graham, M. A. Cane, S. E. Zebiak, S. Dolan, J. J. O'Brien and D. Legler, 1988: On the prediction of the El Niño of 1986-1987. *Science*, **241**, 192-196.
- Battisti, D. S., 1988: Dynamics and thermodynamics of a warming event in a coupled tropical atmosphere-ocean model. *J. Atmos. Sci.*, **45**, 2889-2819.
- Bishop, J.K.B, and W.B. Rossow, 1991: Spatial and temporal variability of global surface solar irradiance. *J. Geophys. Res.*, **96**, 1839-16858.
- Bussalacchi, A., and J. J. O'Brien, 1981: Interannual variability of the equatorial Pacific in the 1960's. *J. Geophys. Res.*, **86**, 10901-10907.
- Cane, M.A., 1984: Modeling Sea level during El-Niño. *J. Phys. Oceanog.*, **14**, 1864-1874.
- Cane, M. A., 1992: Comments on "the fast-wave limit and interannual oscillations". *J. Atmos. Sci.*, **20**, 1947-1949.
- Cane, M.A. and Patton, 1984: A Numerical Model for Low-Frequency Equatorial Dynamics". *J. Phys. Oceanog.*, **14**, 1853-1863.
- Cane, M.A., M. Munnich and S.E.Zebiak,. 1990: A study of self-excited oscillation of the tropical Ocean Atmosphere system. Part 1: linear analysis. *J. Atmos. Sci.*, **47**, 1562-1577.
- Cane, M. A., S. E. Zebiak and S.C. Dolan, 1986: Experimental forecasts of El Niño, *Nature*, **321**, 827-832.
- Chao, Y. and G. S. Philander, 1993: On the structure of the Southern Oscillation. *J. Climate*, Vol 6, n°3, 450-469.

- Chao, Y., D. Halpern, and C. Périgaud, 1993: Sea surface height variability during 1986-1988 in the tropical Pacific ocean. *J. Geophys. Res.*, **98**, 6947-6959.
- Cheney, R. E, and L. Miller, 1988: Mapping the 1986-1987 El Niño with Geosat Altimeter Data, *EOS Transaction AGU* **69**(31), 754-755.
- Cheney, R.E. B.C. Douglas and L. Miller, 1989: Evaluation of Geosat altimeter data with application to tropical Pacific sea level variability. *J. Geophys. Res.*, **94**, 4737-4747.
- Cheney R.E., and L. Miller, 1990: Recovery of the Sea level in the western Pacific from Geosat Altimetry, *J. Geophys. Res.*, **95**, p2977-2984.
- Cheney, R.E., W.J. Emery, B.J. Haines and F. Wentz, 1991: Recent improvements in GEOSAT altimeter data. *EOS Transactions*, AGU, December 17.
- Delcroix, T., J. Picaut, and G. Eldin, 1991: Equatorial Kelvin and Rossby waves evidenced in the Pacific Ocean through Geosat sea level and surface current anomalies. *J. Geophys. Res.*, **96**, Supplement, 3249-3262.
- Delcroix, T., J-P. Boulanger, F. Masia and C. Menkes, 1994: GEOSAT-derived sea level and surface-current anomalies in the equatorial Pacific, during the 1986-1989 El Niño and La Niña. Accepted, *J. Geophys. Res.*.
- Fu, R., Del Genio D., Rossow W.B. and W. T. LIU, 1992: Cirrus-cloud thermostat for tropical sea surface temperatures tested using satellite data. *letters to Nature*, **358**, 394-397.
- Fu, R. and W. T. LIU, 1993: Tropical Cloud-Sea surface temperature Interaction associated with ENSO, submitted to *J. of Climate*.
- Goldenberg, S. B. and J.J. O'Brien, 1981: Time and space variability of tropical Pacific wind stress. *Mon. Wea. Rev.*, **109**, 1190-1207.

Graham, N. E., and W. B. White, 1988: The El Niño cycle: a natural oscillator of the Pacific ocean-atmosphere. *Science*, **240**, 1293-1302.

Graham, N. E., and W. B. White, 1990: The role of the western boundary in the ENSO cycle: experiments with coupled models. *J. Phys. Oceanog.*, 1935-1948.

Jin, F. F., and J. D. Neelin, 1993: Modes of interannual tropical ocean-atmosphere interaction-A unified view. Part I: Numerical results. *J. Atmos. Sci.*, **50**, (21) in press.

Kessler, W. S., 1990: Observations of Long Rossby waves in the Northern Tropical Pacific, *J. Geophys. Res.*, **95**, 5183-5217.

Kindle J.C. and P.A. Phoebus, 1994: The ocean response to operational wind bursts prior to and during the 1991-1992 El Niño, Ocean Sciences meeting abstracts, *EOS Transactions*, Am. Geophys. Union (0096-3941), p113.

Latif, M., A. Sterl, E. Maier-Reimer, and M. M. Junge, 1993: Climate variability in a coupled GCM. Part I: The tropical Pacific. *J. Climate*, **6**, 21.

Liu, W.T., 1988: Moisture and latent heat flux variabilities in the tropical Pacific derived from satellite data. *J. Geophys. Res.*, **93**, 6749-6760.

Liu, W.T., J.K. Bishop, W. Rossow and K. Case, 1993: Monthly maps of Ocean Surface thermal forcing. *JPL Publication 93-13*, pp.

Lukas R., Hayes SP, and K. Wyrski, 1984: Equatorial sea level response during the 1982-1983 El Nino, *J. Geophys. Res.*, **89**, 10425-10430.

McCreary J.P., 1984: Equatorial beams, *J. Mar. Res.*, **42**, 395-430.

Miller, 1993: Blending Altimetry and tide-gauge data, Report of the SWT Verification workshop, Jet Propulsion Laboratory, Pasadena, CA91109.

Miller L. and R.E. Cheney, 1990: Large-scale Meridional Transport in the tropical Pacific Ocean during the 1986-1987 El Niño From Geosat, *J. Geophys. Res.*, **95**, 17905-17919.

Moore, D. W., and S. G. H. Philander, 1977: Modeling of the tropical ocean circulation. (Chap. 8), *The sea*, Vol. 6, E. D. Goldberg, I. N. Cave, J. J. O'Brien and J. H. Steek, Eds., Interscience, 1048 pp.

Neelin, J. D., 1991: The slow sea surface temperature mode and the fast-wave limit: Analytic theory for tropical interannual oscillations and experiments in a hybrid coupled model. *J. Atmos. Sci.*, **48**, 584-606.

duPenhoat, Y., T. Delcroix and J. Picaut, 1992: Interpretation of Kelvin and Rossby waves in the equatorial Pacific from model-Geosat intercomparison during the 1986-1987 El Niño. *Oceanol. Acta*, **15**, 545-554.

Picaut, J., A. Busalacchi, M. Mc Phaden, B. Camusat, 1990: Validation of the geostrophic method for estimating zonal currents at the equator from Geosat altimetric data. *J. Geophys. Res.*, **95**, 3015-3024.

Rasmusson, E. M., and T. H. Carpenter, 1982: Variations in tropical sea surface temperature and surface wind fields associated with the Southern Oscillation/El Niño. *Mon. Wea. Rev.*, **110**, 354-384.

Reynolds, R. W., 1988: A real-time global sea surface temperature analysis. *J. Climate*, **1**, 75-86.

Schopf M.J. and M.J. Suarez, 1988: Vacillations in a coupled ocean-atmosphere system, *J. Atmos. Sci.*, **45**, 3283-3287.

Tourre, Y., and W. White, 1994: ENSO signals in global upper ocean thermal structures. submitted to *J. Phys. Oceanog.*

White, W. B., N.E. Graham and C.K. Tai, 1990: Satellite observations of Rossby wave reflection at the maritime western boundary of the tropical Pacific. *J. Geophys. Res.*, **95**, 3101-3116.

Zebiak, S. E., 1985: Tropical Atmosphere-Ocean Interaction and the El Niño-Southern Oscillation phenomenon. PhD theses at MIT, 261 pp.

Zebiak, S. E., and M.A. Cane, 1987: A model El Niño-Southern Oscillation. *Mon. Wea. Rev.*, **115**, 2262-2278.

Zebiak, S. E., 1989: Oceanic heat content variations and El Niño cycles. *J. Phys. Oceanog.*, 475-486.

Zebiak, S. E., 1993: Air-sea interaction in the equatorial atlantic region. *J. Climate*, Vol. 6, N°8, 1567-1586.

## Figure Captions

Figure 1: FSU zonal stress as a function of longitude along the equator and time between February 1980 and April 1993. Units are  $\text{dyn/cm}^2$ . Shaded zones correspond wind-stress anomalies smaller than  $-0.2 \text{ dyn/cm}^2$  and zones with "+" to anomalies larger than  $+0.2 \text{ dyn/cm}^2$ .

Figure 2: Sea level simulated by the CR as a function of time between February 1980 and April 1993. Units are cm. Shaded zones correspond to sea level anomalies smaller than  $-5 \text{ cm}$  and zones with "+" to anomalies larger than  $+5 \text{ cm}$ . Figure 2a is the section along the equator. Figure 2b is the zonally averaged meridional section. Figures 2c and 2d are zonal sections meridionally averaged over  $5^\circ\text{N}-15^\circ\text{N}$  and over  $5^\circ\text{S}-15^\circ\text{S}$  respectively.

Figure 3: Same as Figure 2 for the observed sea level derived from Geosat between April 1985 and September 1989.

Figure 4: Same as Figure 2 for the observed sea level derived from the XBT data between February 1980 and August 1992.

Figure 5: Sea level (in cm) as a function of time (in years). The top panel corresponds to the average over NINO3 ( $5^\circ\text{S}-5^\circ\text{N}$ ,  $90^\circ\text{W}-150^\circ\text{W}$ ) and the bottom panel to the average over the western Pacific ( $135^\circ\text{E}-152.5^\circ\text{E}$ ;  $5^\circ\text{S}-5^\circ\text{N}$ ). The plain line is for the XBT, the dashed line for the CR and the dotted line for Geosat.

Figure 6: Sea level variability over April 1985-September 1989 as a function of longitude. Plots have been averaged in the  $3^\circ\text{S}-3^\circ\text{N}$  band. The plain line corresponds to the CR, the dashed line to Geosat and dotted/dashed line to the XBT.

Figure 7: Sea surface temperature anomaly as a function of longitude along the equator and time in years. Units are  $^\circ\text{C}$ . Shaded zones

correspond to SST anomalies smaller than  $-1^{\circ}\text{C}$  and zones with "+" to anomalies larger than  $+1^{\circ}\text{C}$ . Results are derived from (a) the CR between February 1980 and April 1993 , (b) the AVHRR data between January 1982 and August 1991 and (c) the XBT data between February 1980 and July 1992.

Figure 8: NINO3 averaged SST and sea level as a function of time. Top panel (a) corresponds to simulations and bottom (b) to observations. For Figure 8a, SST is in full line and sea level in dashed line. For Figure 8b, SST from AVHRR is in plain line, SST from XBT in dotted line and sea level from XBT heat content in dashed line. SST is in  $^{\circ}\text{C}$  and sea level in cm has been multiplied by 0.15.

Figure 9: SST rate of change and zonal advection of temperature as a function of time. The plain line corresponds to  $\partial\text{SST}/\partial t$  and the dashed line corresponds to the sum: term(1) + term(2) defined in section 5.4. All terms have been averaged over NINO4. Units are  $^{\circ}\text{C} (10\text{days})^{-1}$ . Results are derived from the CR.

Figure 10: Zonal current anomaly as a function of longitude along the equator and time between February 1980 and April 1993. Units are cm/s. Shaded zones correspond to current anomalies smaller than  $-15$  cm/s and zones with "+" to anomalies larger than  $+15$  cm/s. Results are derived from the CR (a), from the run O.BNDY0 (b), and from the run O.FRIC (c).

Figure 11: Energy spectrum of the zonal current anomalies averaged over the NINO4 box. The spectrum has been computed over 1980-1993. Plain line corresponds to the CR, dotted line to run O.BNDY0 and dashed line to run O.FRIC. Units are  $1 (\text{cm/s})^2$  per month.

Figure 12: Zonal current anomalies as a function of longitude along the equator and time between April 1985 to September 1989. Results are derived from Geosat and represent: (a) the Kelvin component, (b) the Rossby component, (c) their sum. Units and shading are the same as in Figure 10.

Figure 13: Energy spectrum of the zonal current anomalies averaged over the NINO4 box. The spectrum has been computed over 1985-1989. Plain line corresponds to the CR, dashed line to run O.BNDY0 and dashed-dotted line to run O.FRIC and heavy dashed line to altimetric currents. Units are  $1 \text{ (cm/s)}^2$  per month.

Figure 14: Same as Figure 9 for the observations, e.g. AVHRR SST anomalies and altimetric anomalous zonal currents.

Figure 15: Same as Figure 1 for the zonal stress simulated in the CR.

Figure 16: NINO3 averaged SST and NINO4 averaged zonal wind stress as a function of time. Top panel corresponds to the results simulated in the CR (a), bottom panel to the observations (b). For Figure 16a, SST is in plain line and wind stress in dashed line. For Figure 16b, wind stress is in dashed line, SST is in plain line for AVHRR and in dotted line for XBT. SST is in  $^{\circ}\text{C}$  and wind stress in  $\text{dyn/cm}^2$  has been multiplied by 5.

Figure 17: Variability of the curl over 1980-1993 as a function of longitude. The dashed lines correspond to observations and the plain lines to the CR. Plots are averaged in the  $3^{\circ}\text{N}-9^{\circ}\text{N}$  band (top) or in the  $3^{\circ}\text{S}-9^{\circ}\text{S}$  band (bottom). Units are  $10^{-7} \text{ Pa/m}$ .

Figure 18: Atmospheric forcing term as a function of longitude along the equator and time. Results are derived from: (a) the CR between February 1980 and April 1993, (b) the observed cloud convection

between July 1983 and December 1990. Units are  $50 \text{ m}^2\text{s}^{-3}$ . The sign convention is that negative anomalies correspond to increased convection and to the atmosphere gaining heat.

FSU

Apr. 93

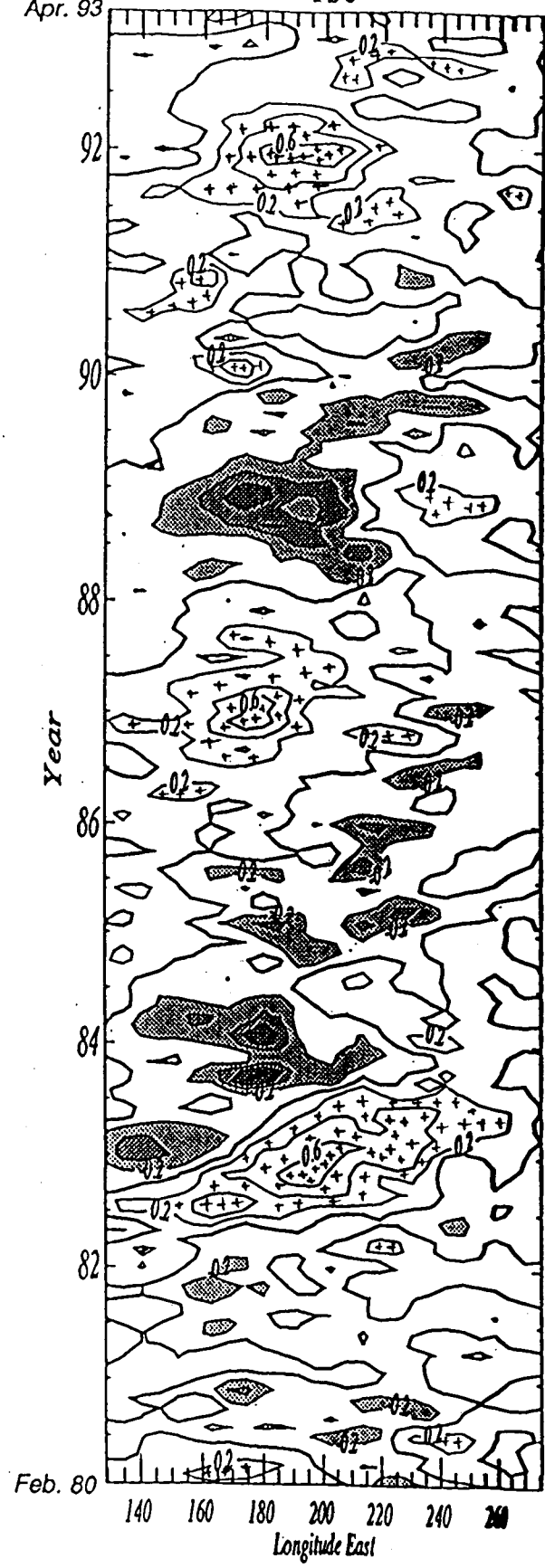


Fig. 1

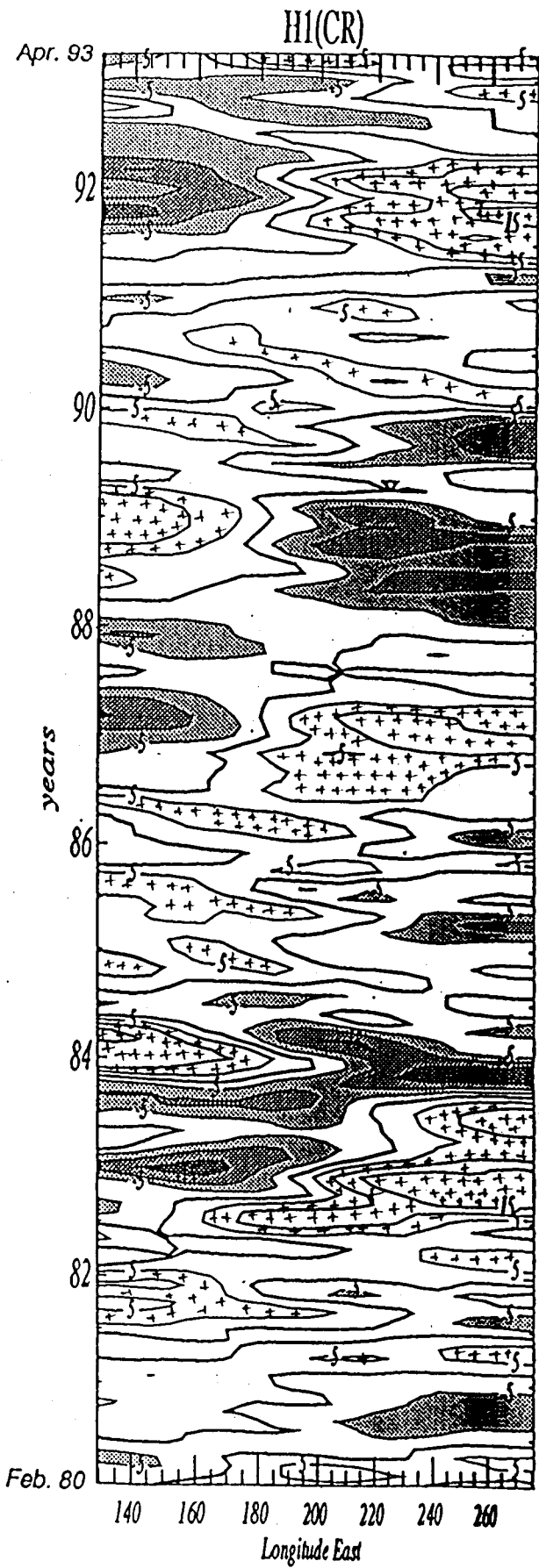


Fig. 2a

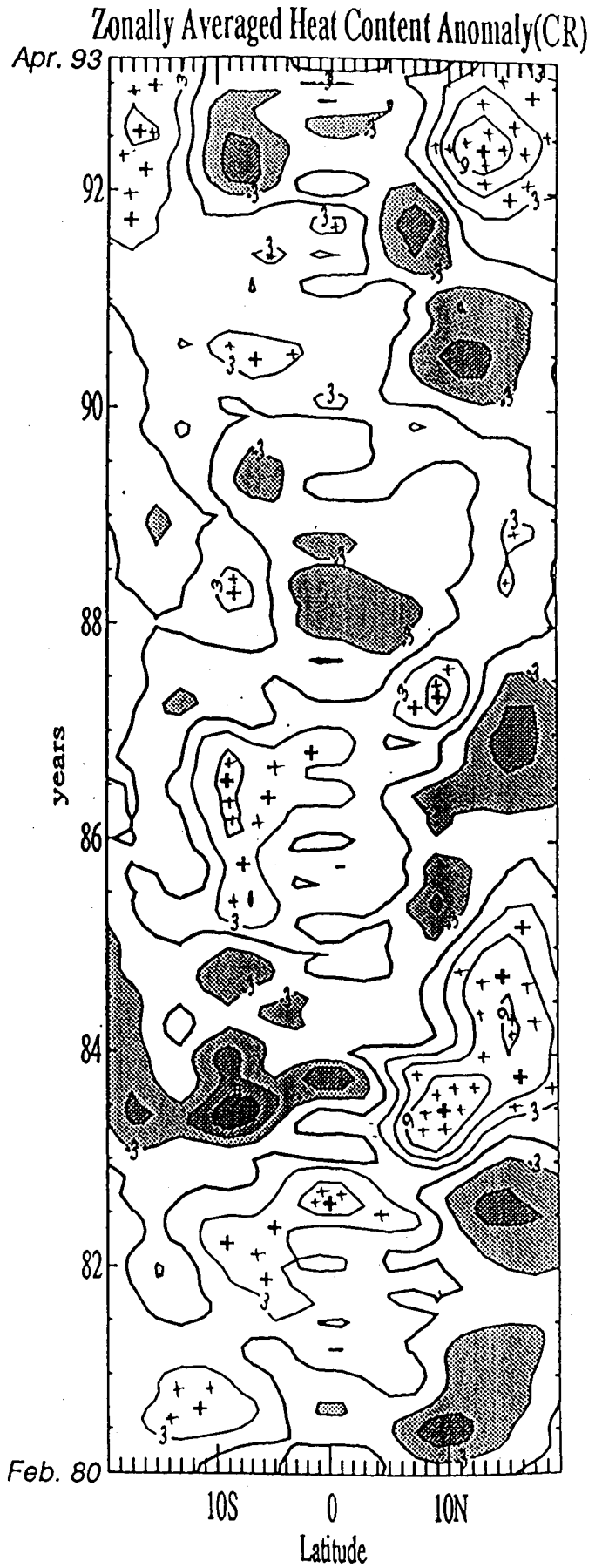
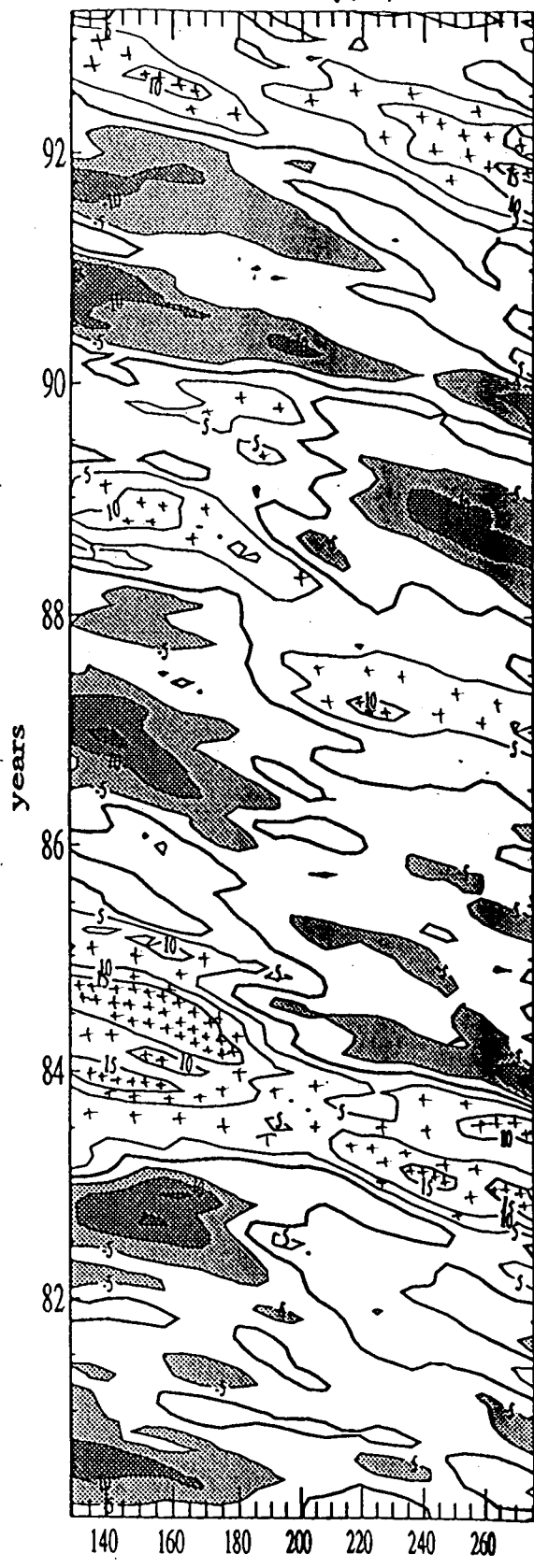


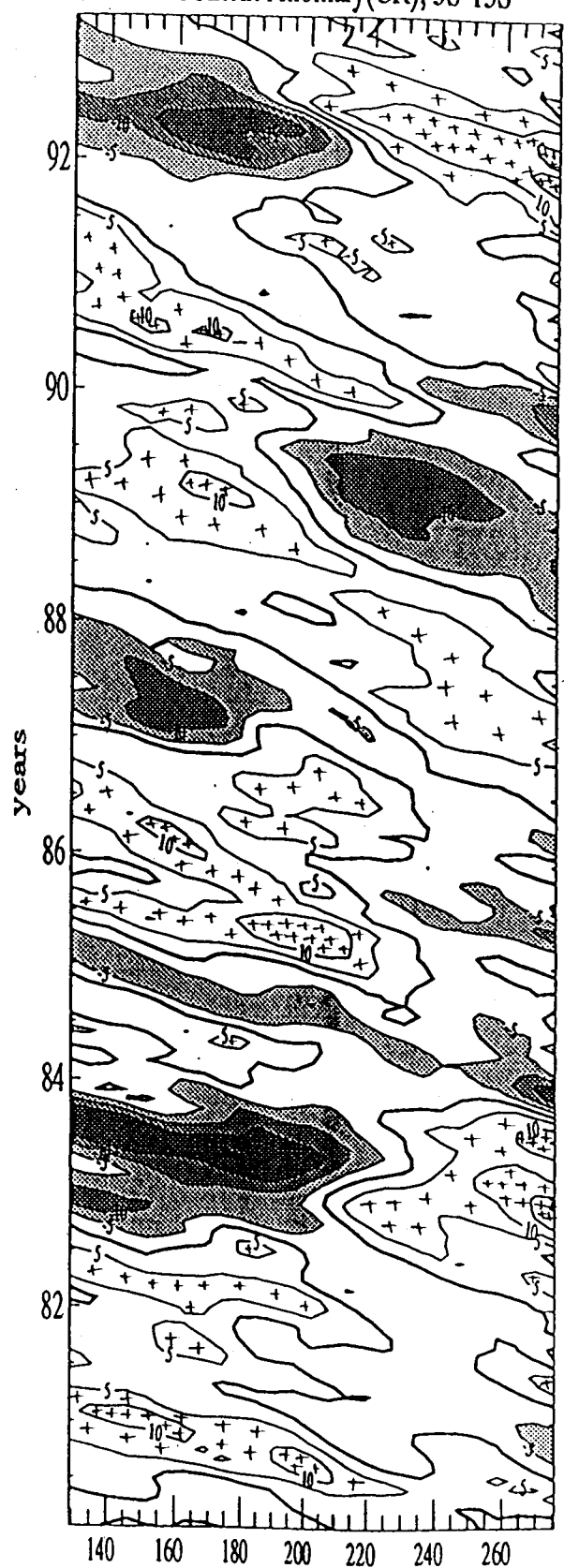
Fig. 2b

Heat Content Anomaly(CR); 5N-15N



Longitude  
Fig 2c

Heat Content Anomaly(CR); 5S-15S



Longitude  
Fig 2d

### GEOSAT

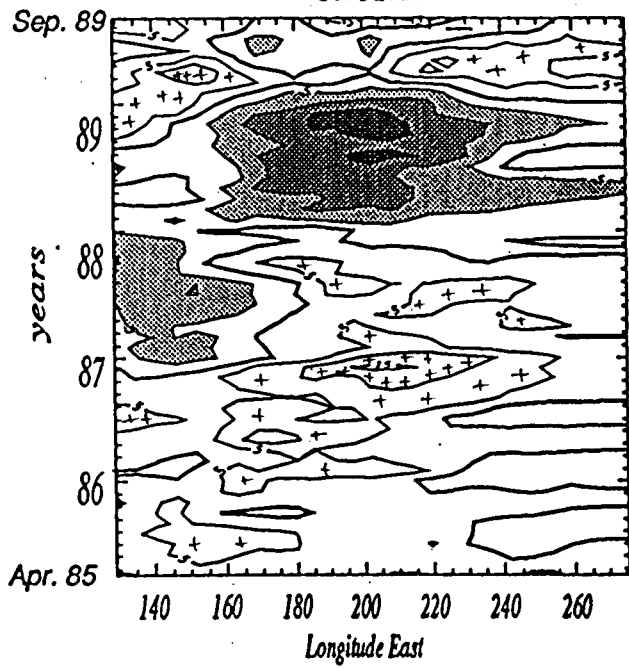


Fig. 3a

### Zonally Averaged Heat Content Anomaly(Geosat)

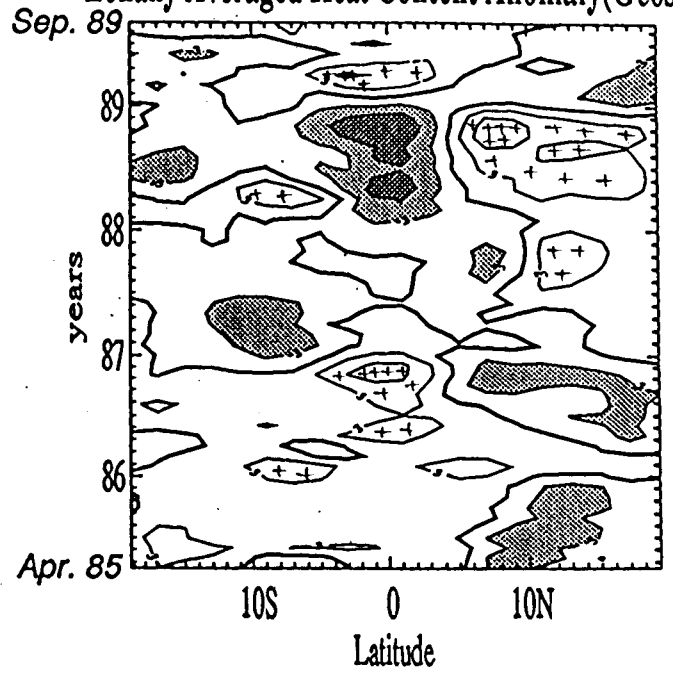


Fig 3 b .

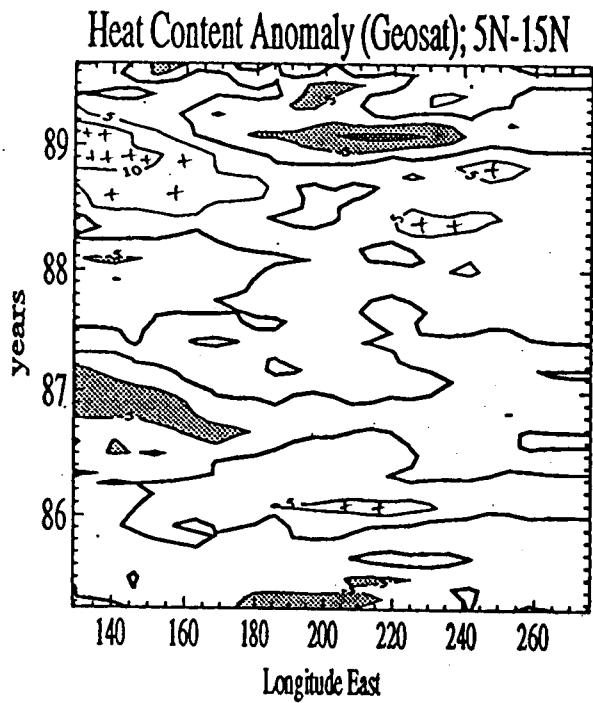


Fig 3c

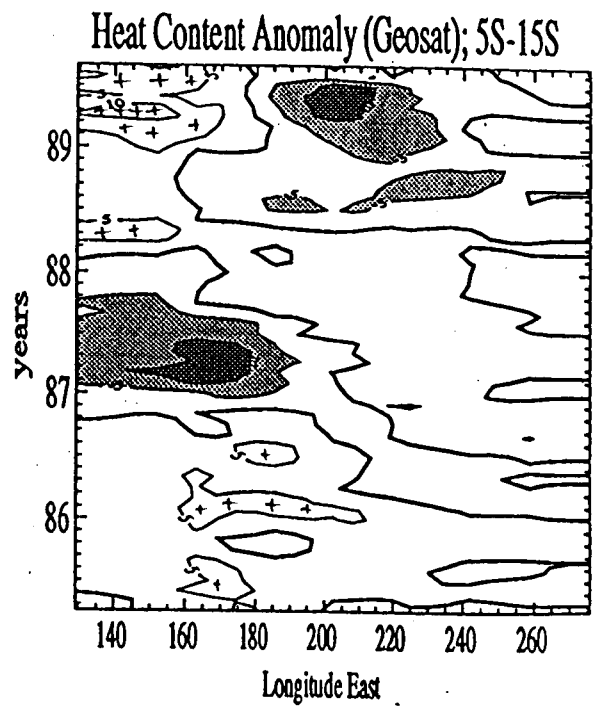


Fig 3d

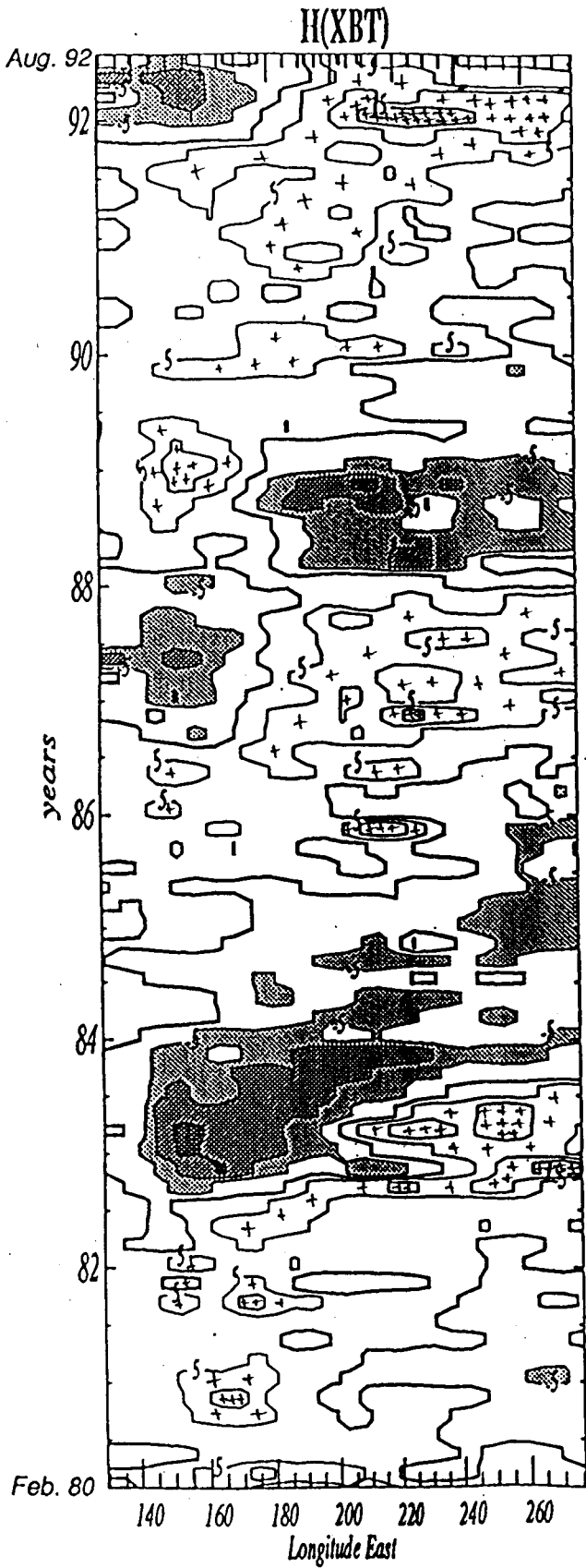


Fig. 4a

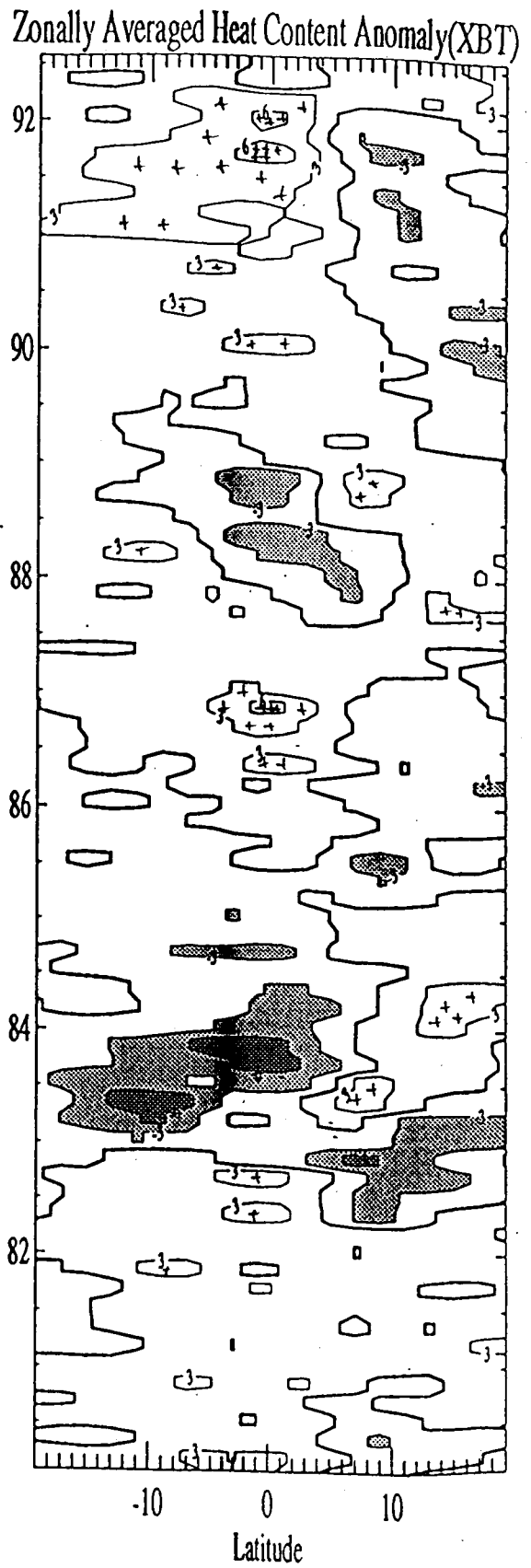
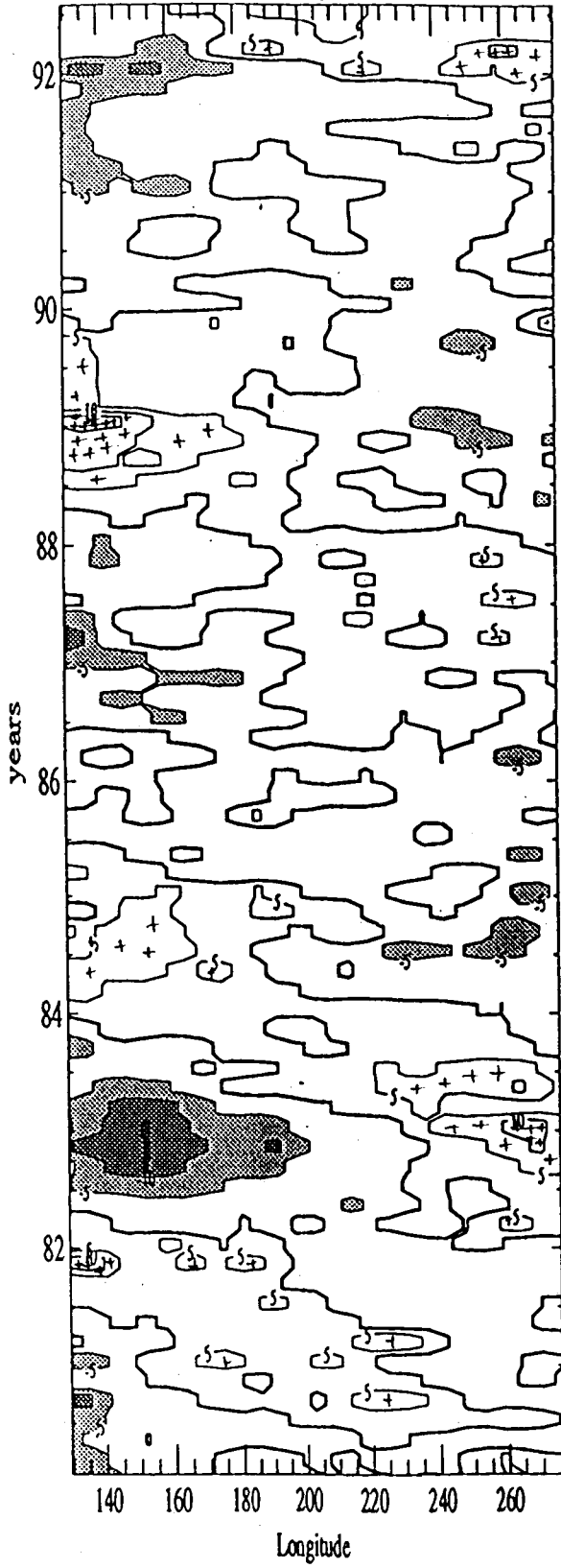


Fig. 4b

Heat Content Anomaly(XBT); 5N-15N



Heat Content Anomaly(XBT); 5S-15S

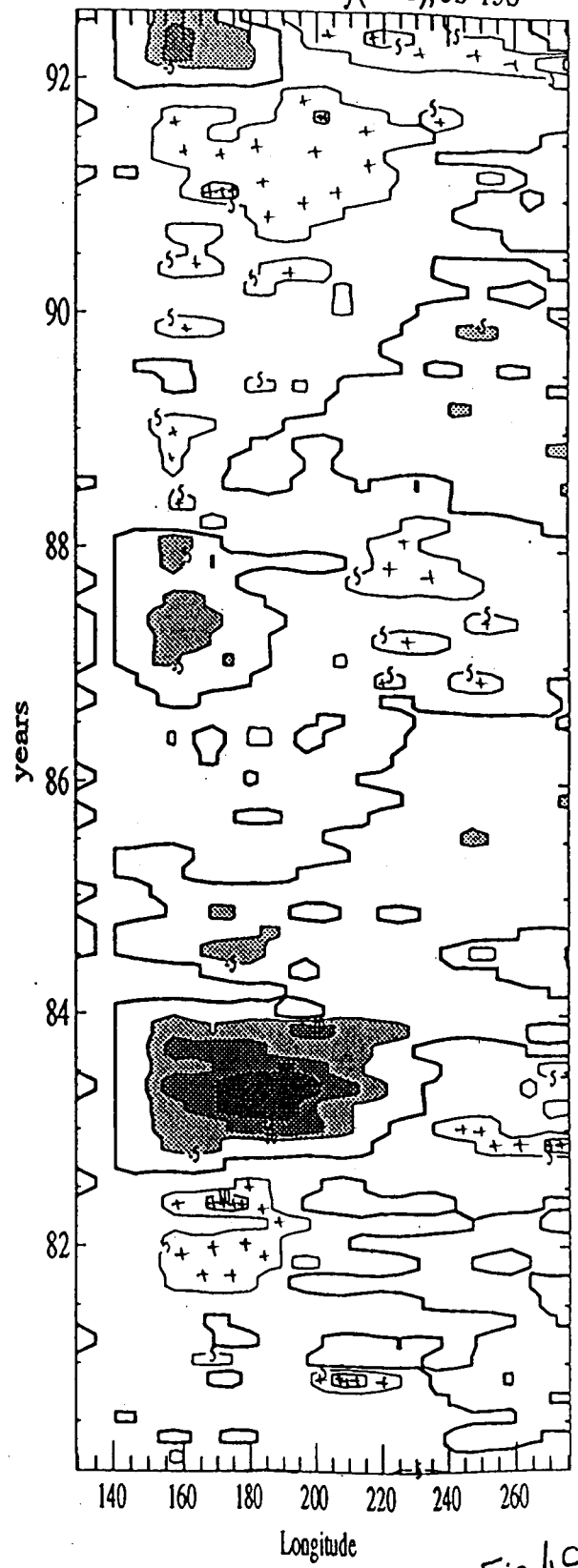


Fig 4cd

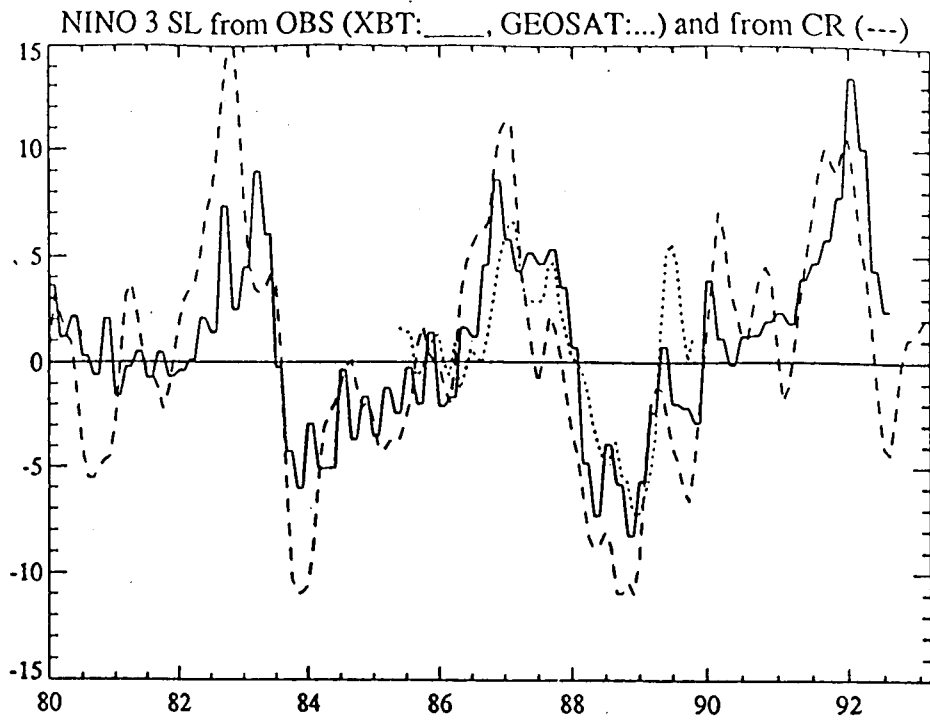


Fig. 5a

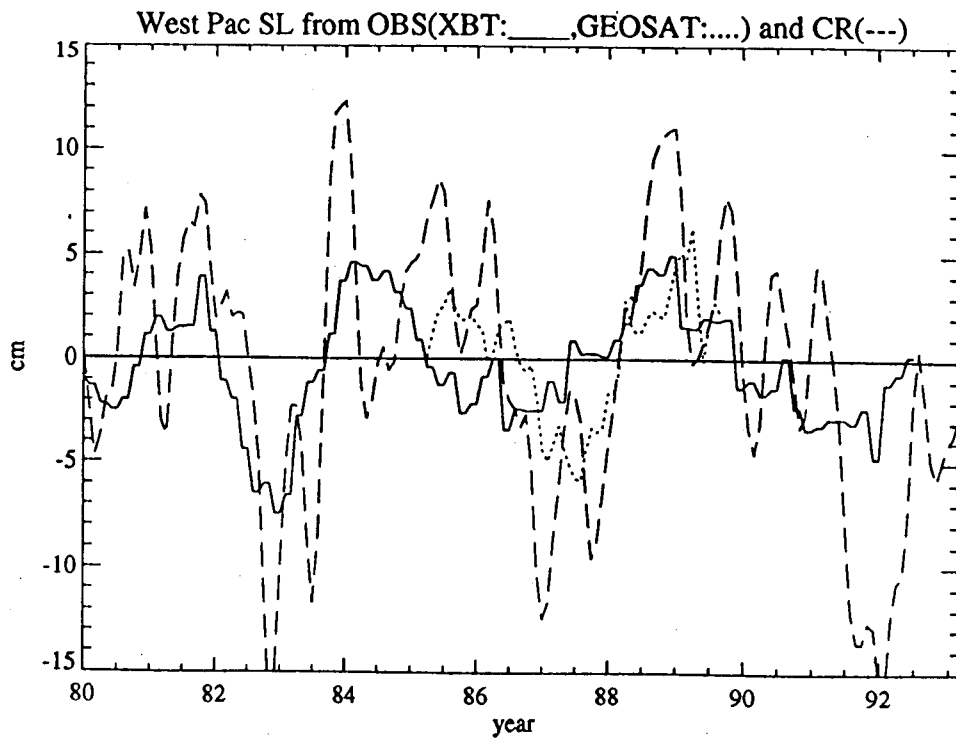


Fig. 5b

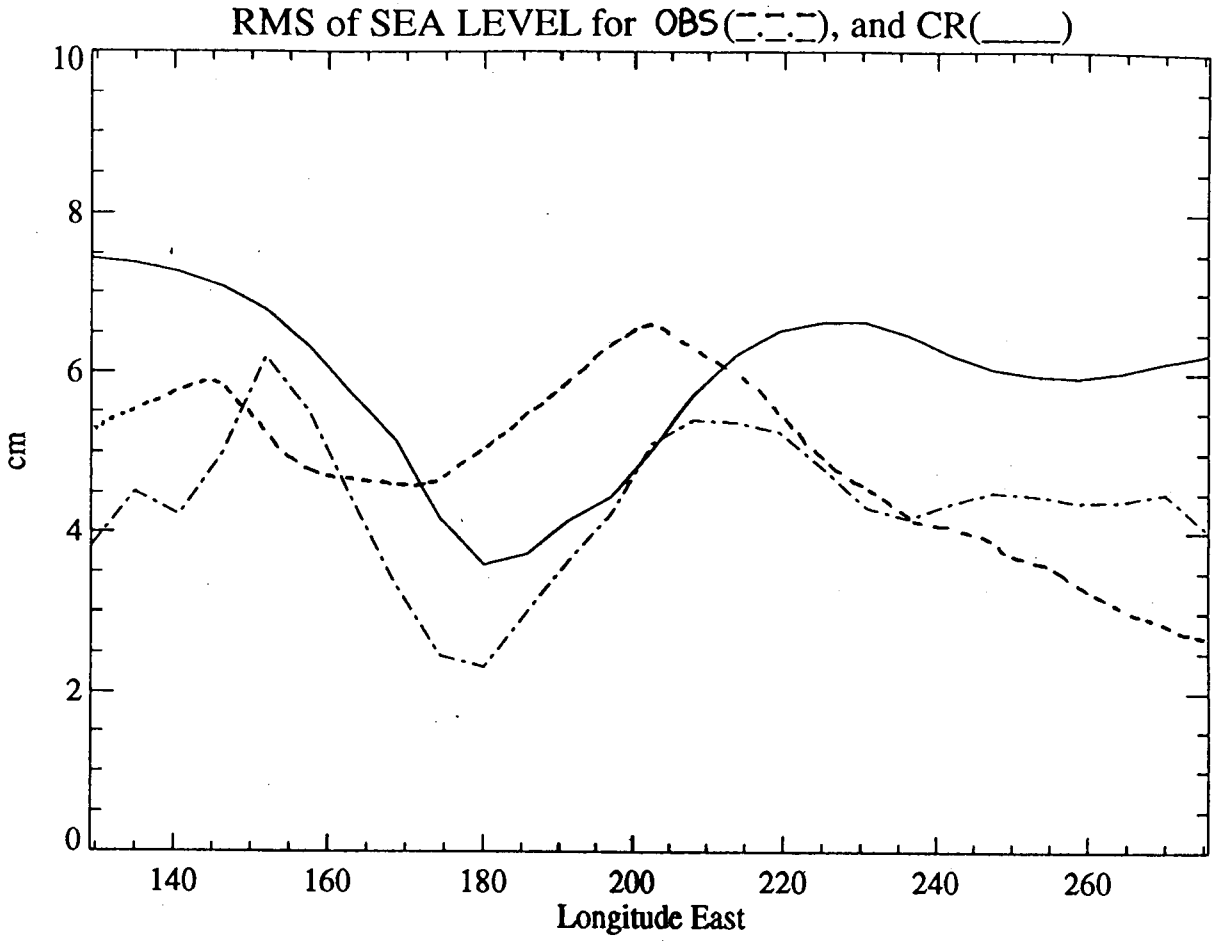


Fig 6

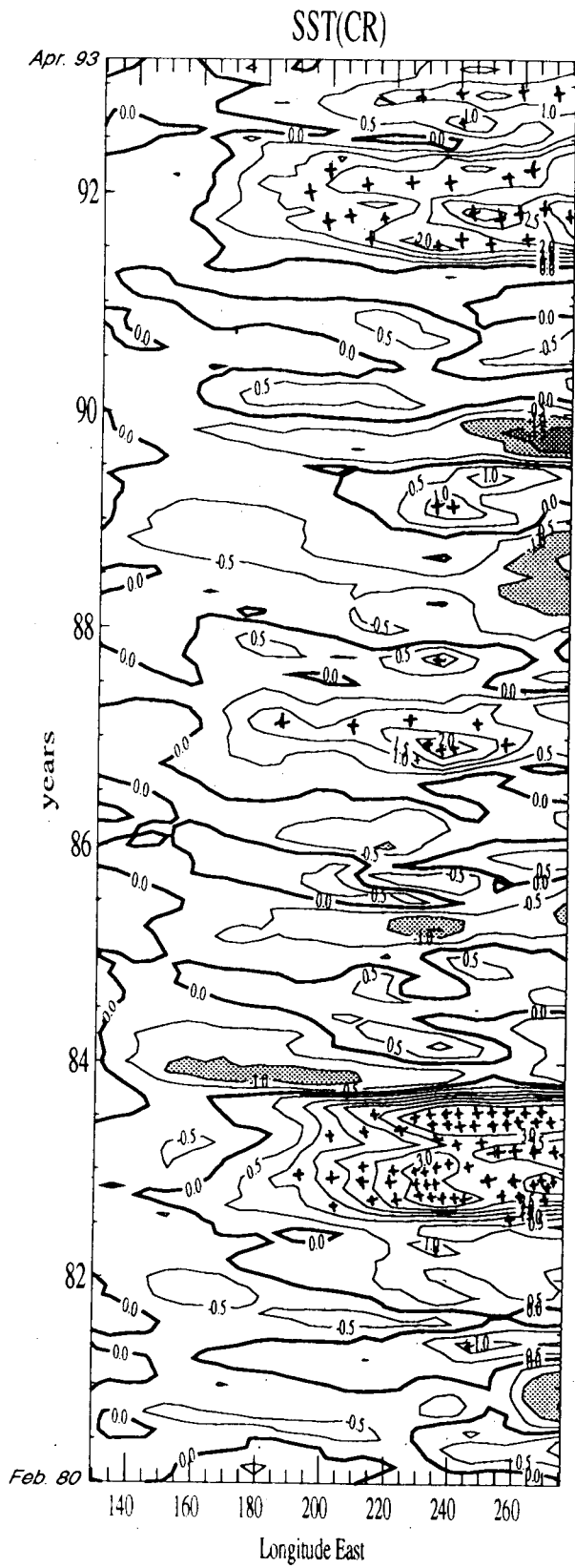


Fig 7a

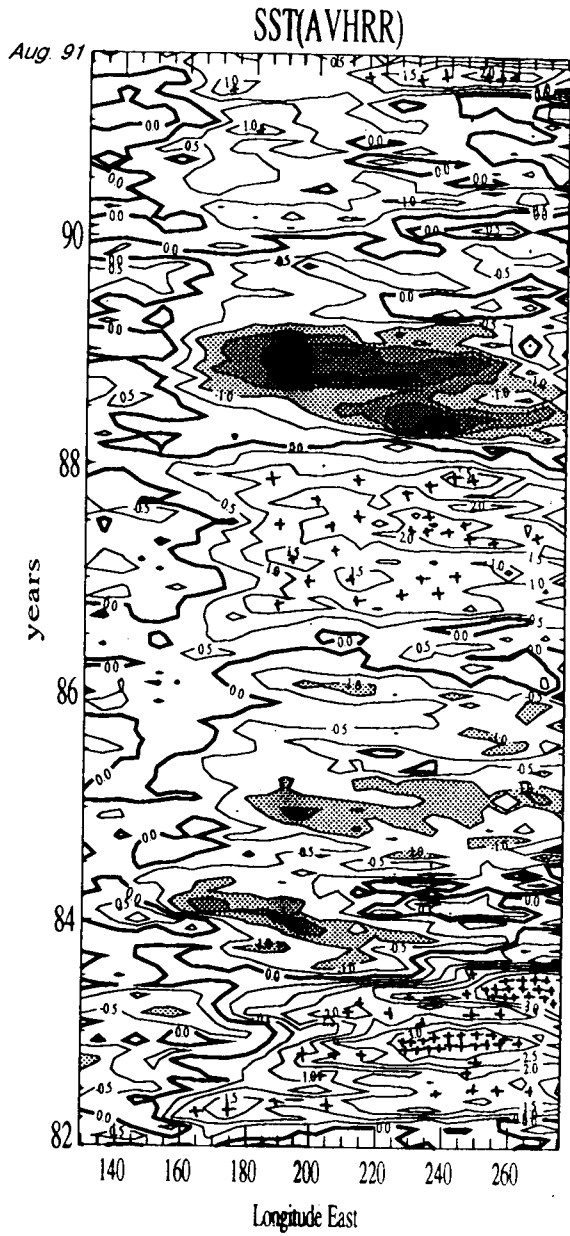


Fig 7b

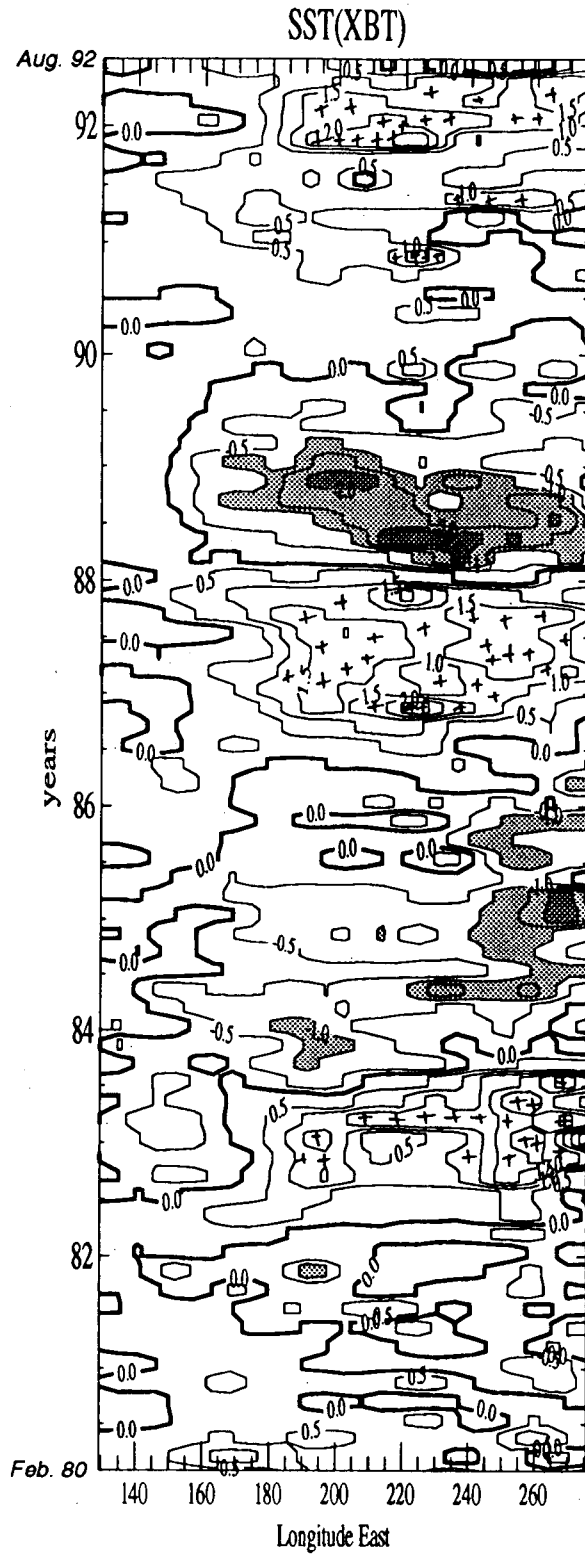


Fig 7c

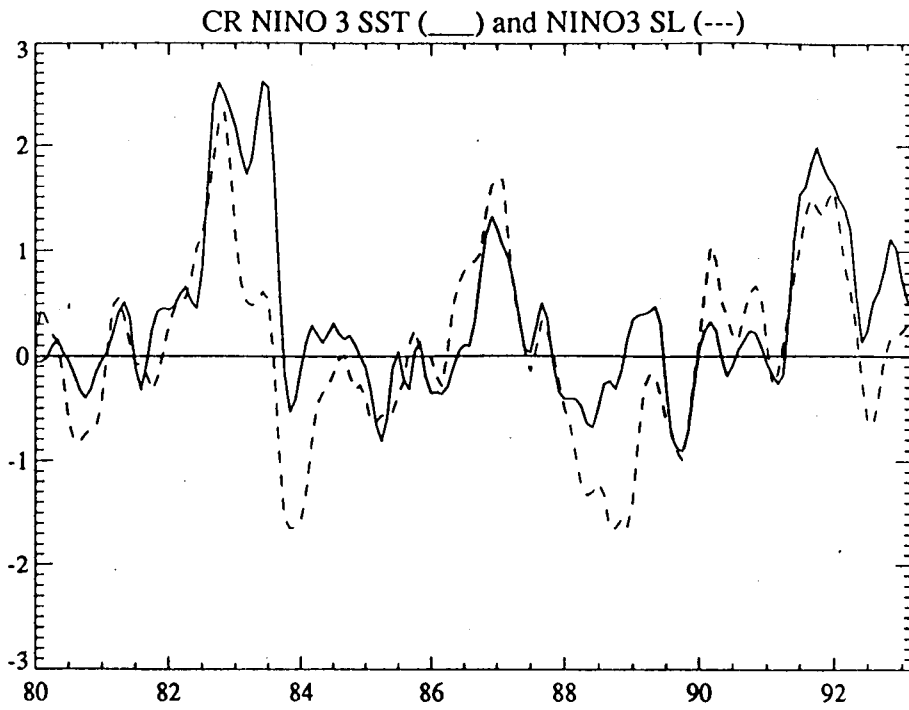


Fig. 8a

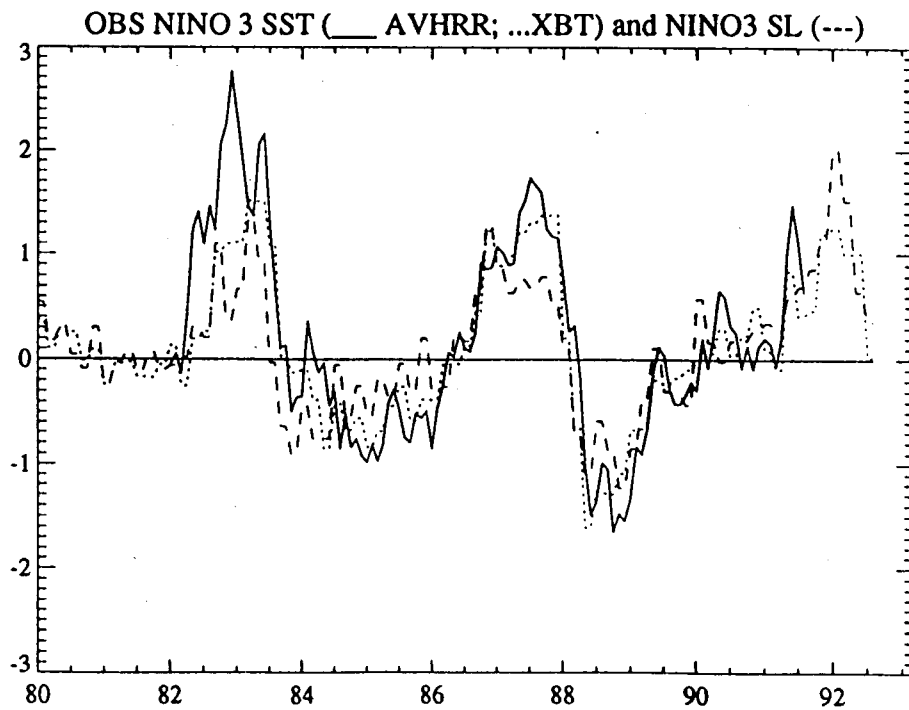


Fig. 8b

CR:  $\partial T/\partial t$  (\_\_\_) and  $-U_0^* \partial T_{tot}/\partial x - U_{clim}^* \partial T/\partial x$  (.....) over NINO4.

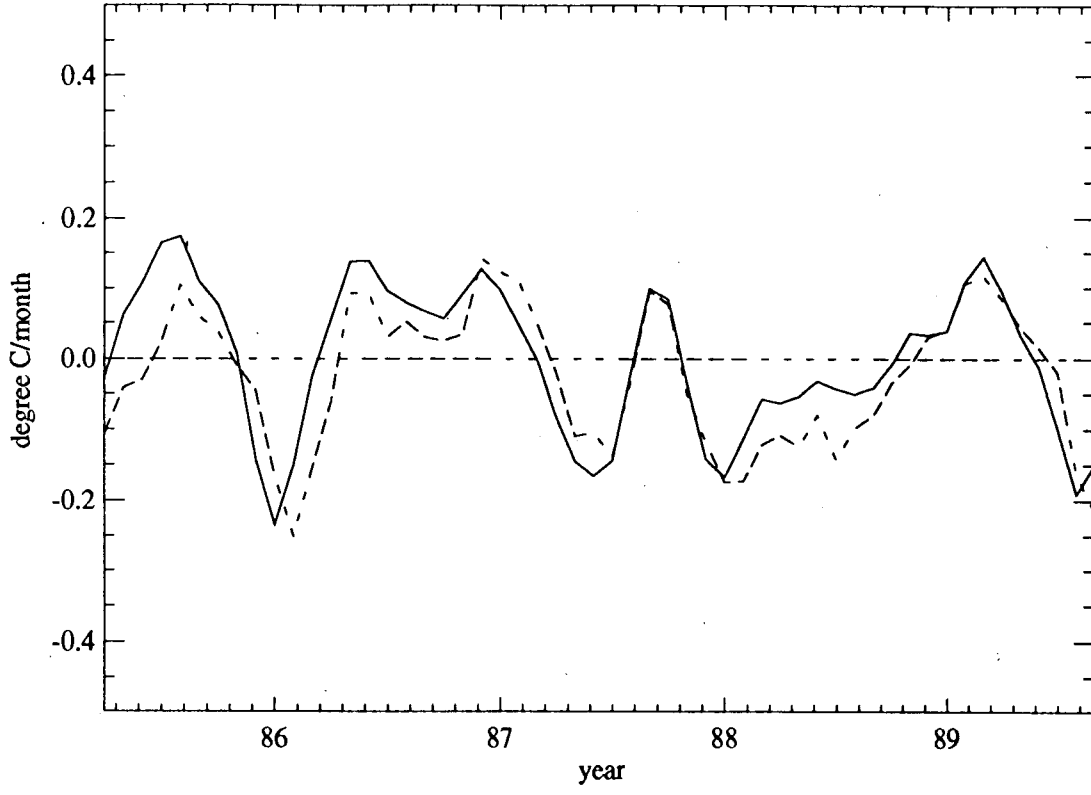


Fig. 9

UI(CR)

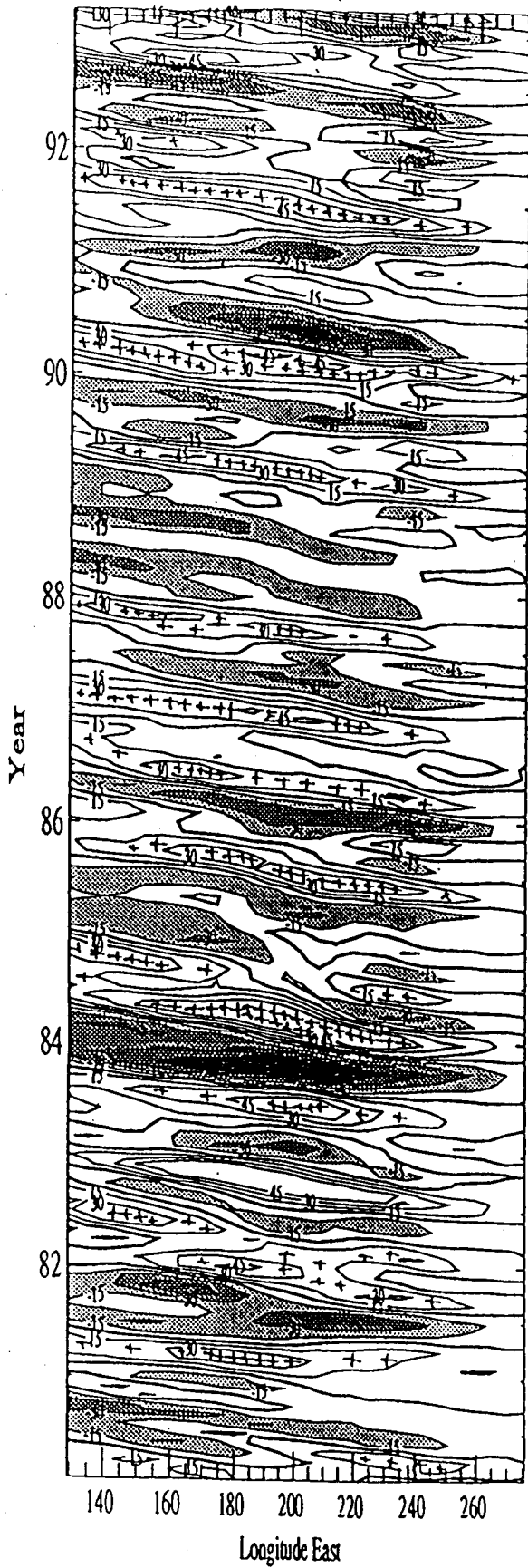


Fig 10 a

UI (Run O.BNDY0)

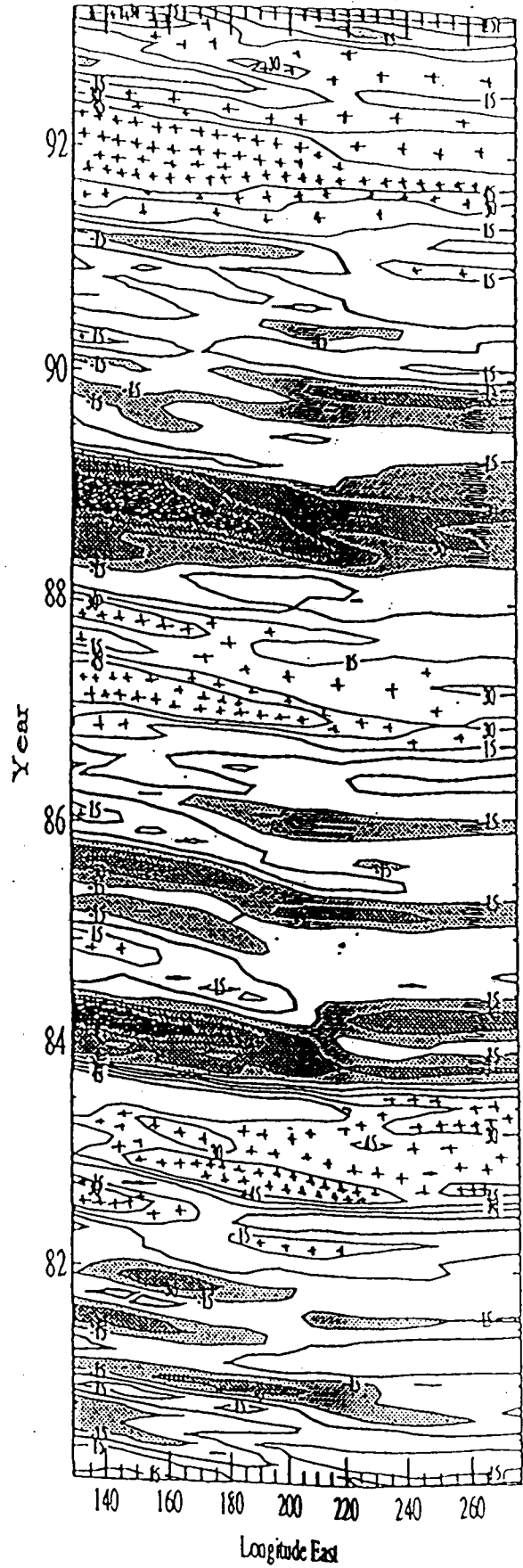


Fig 10 b

# U1(O.FRIC)

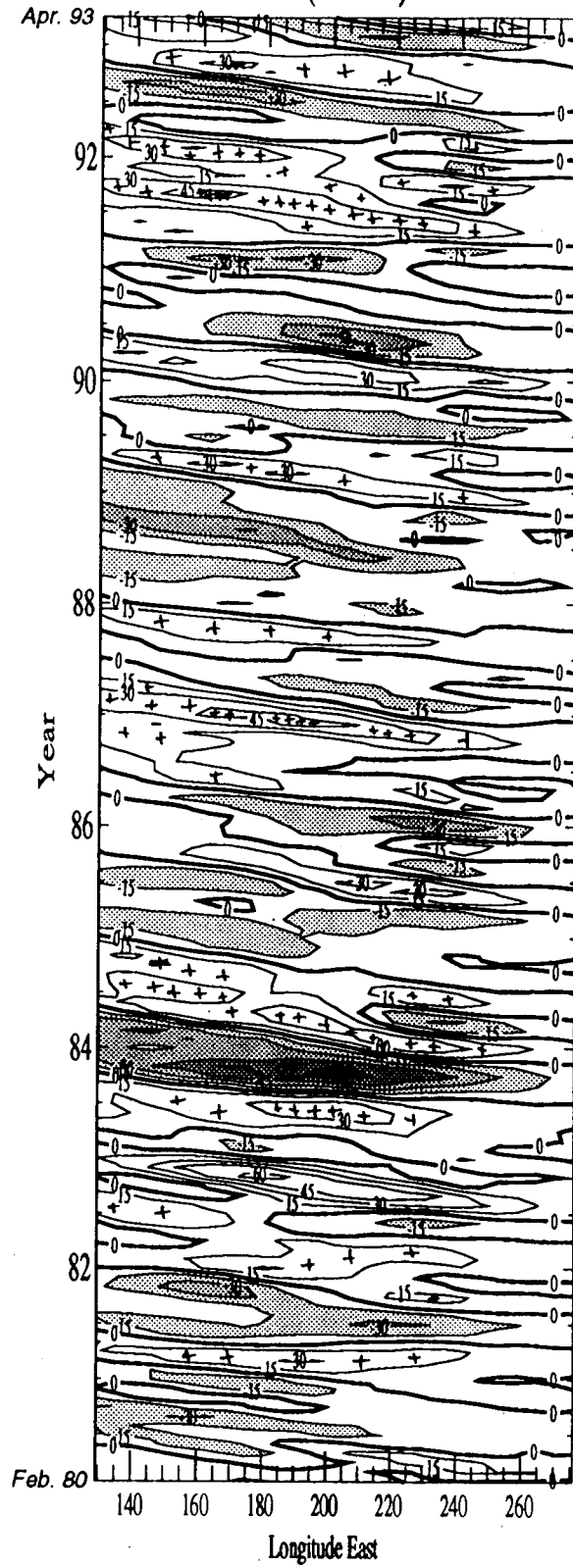


Fig. 10 c

NINO4 averaged zonal flow

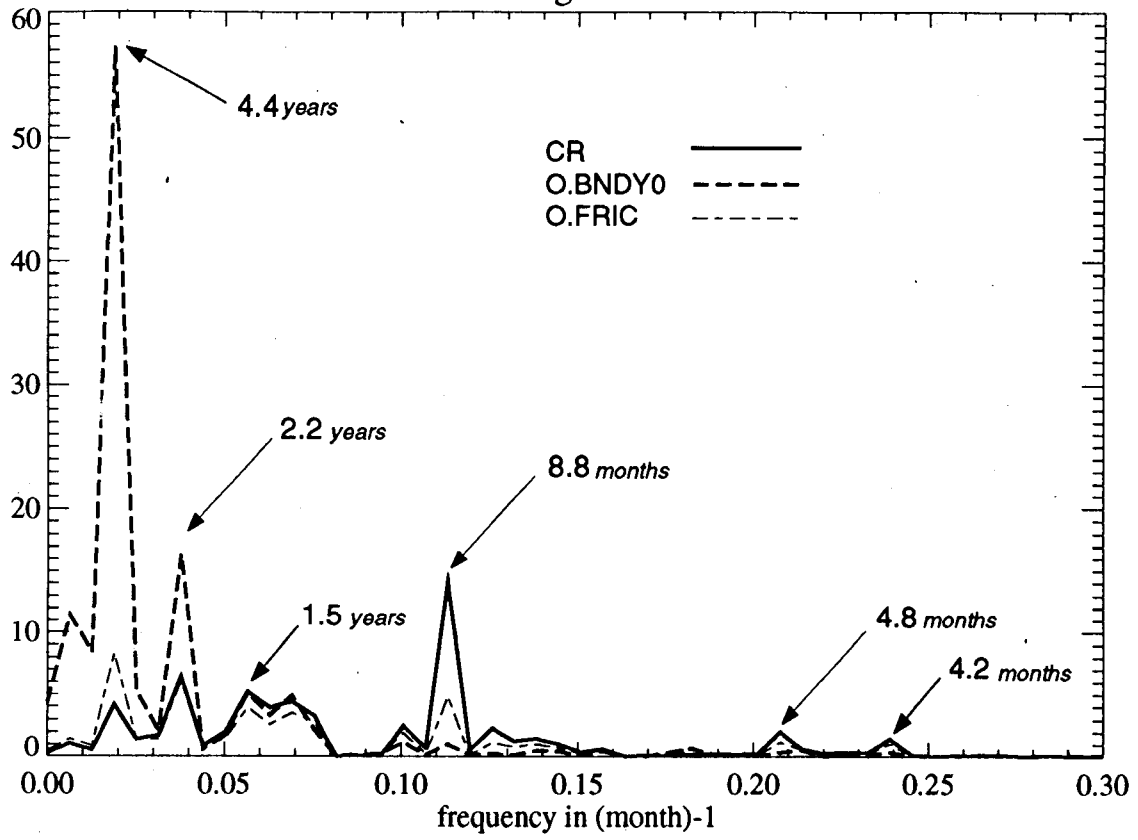
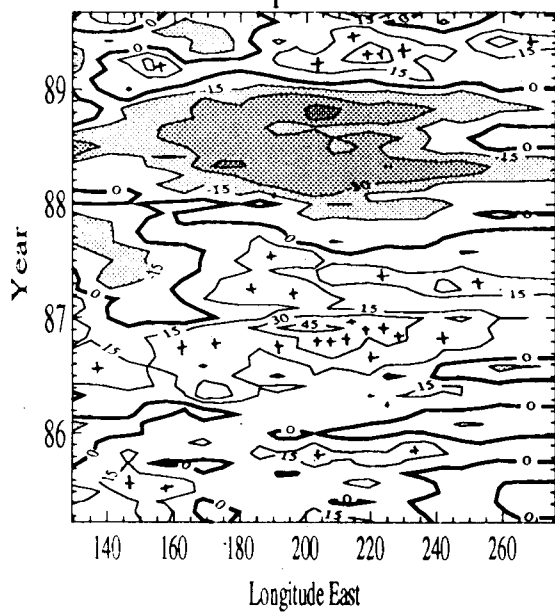
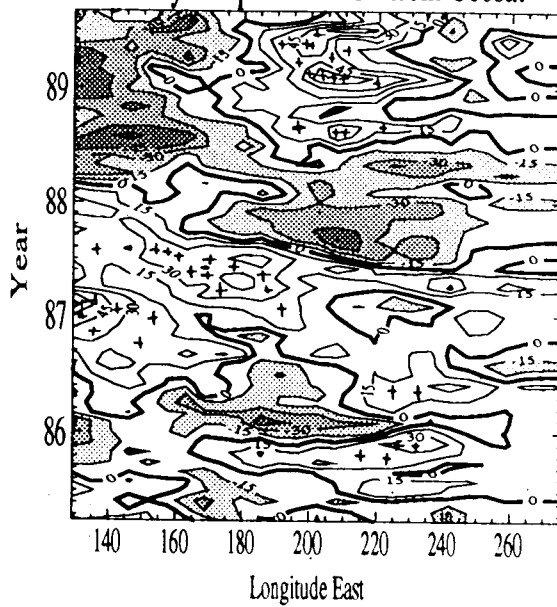


Fig 11

Kelvin component from Geosat



Rosby component of UI from Geosat



UI(GEOSAT)

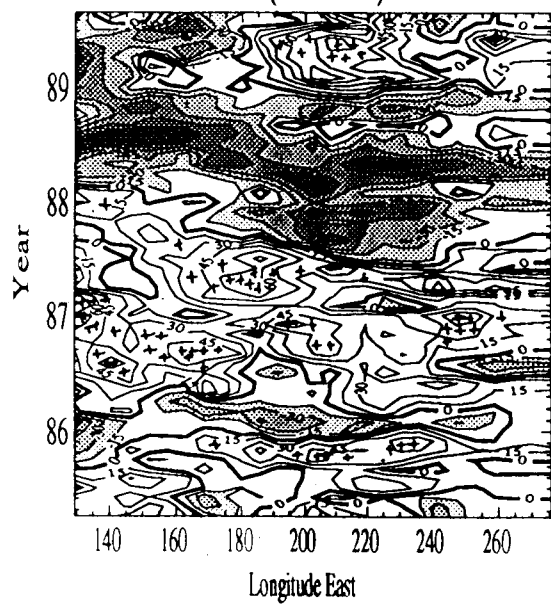


Fig 12a, b, c

NINO4 averaged zonal flow

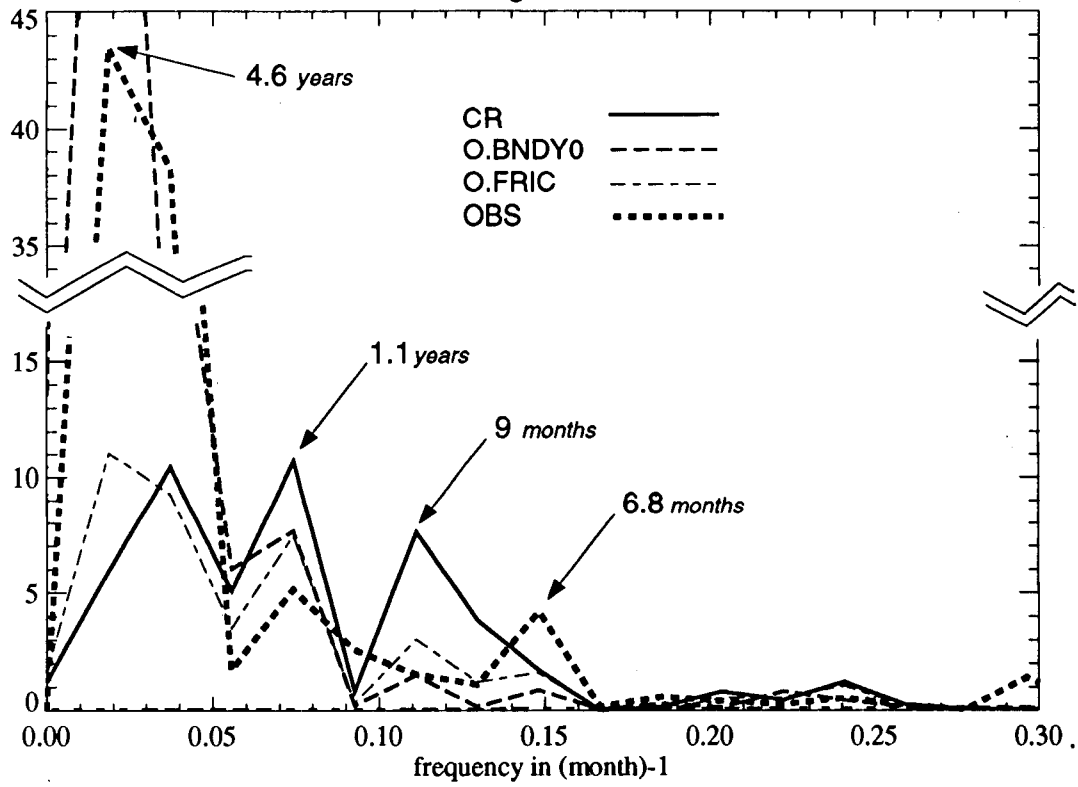


Fig 13

OBS:  $dT/dt$  (\_\_\_),  $-U_0*dT_{tot}/dx(...)$  and  $-U_{clim}*dT/dx(---)$  over NINO4.

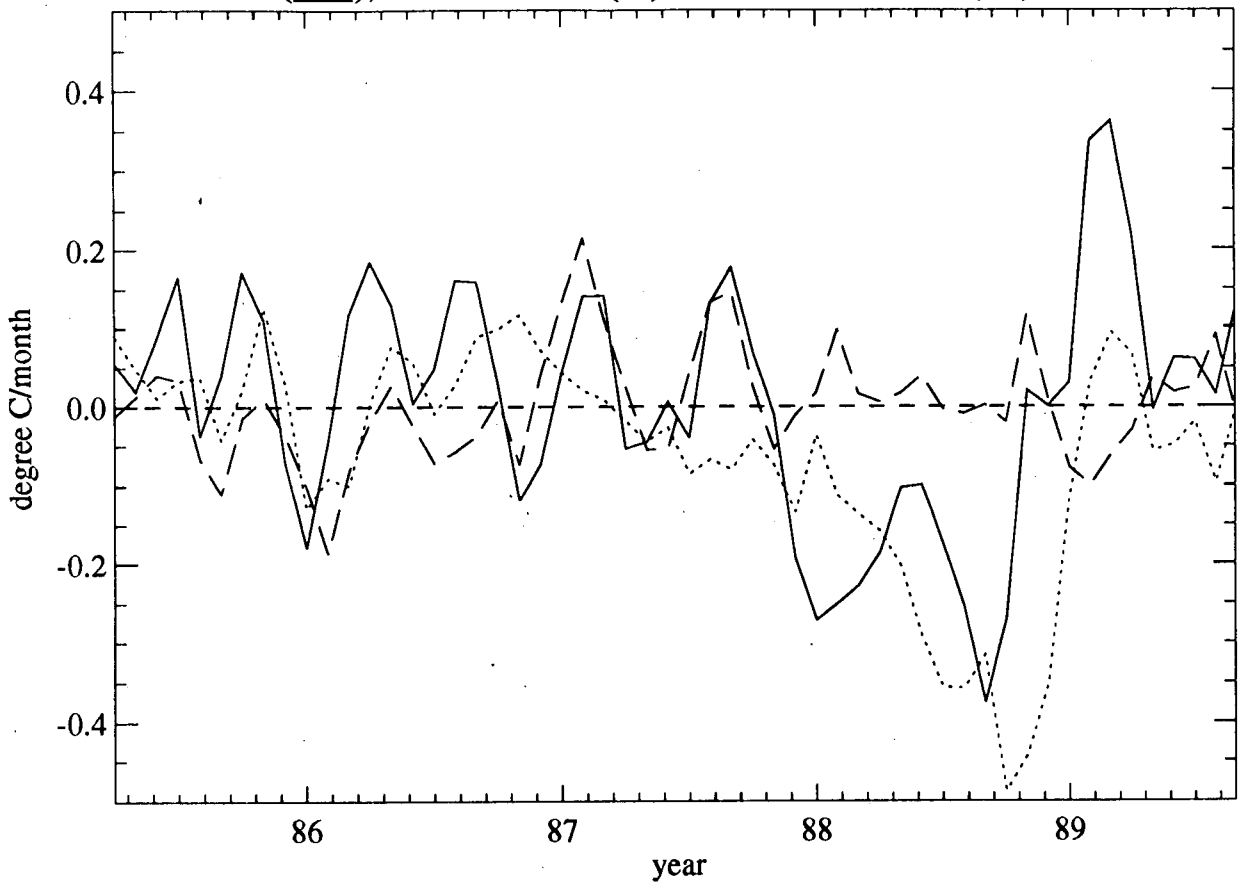


Fig 14

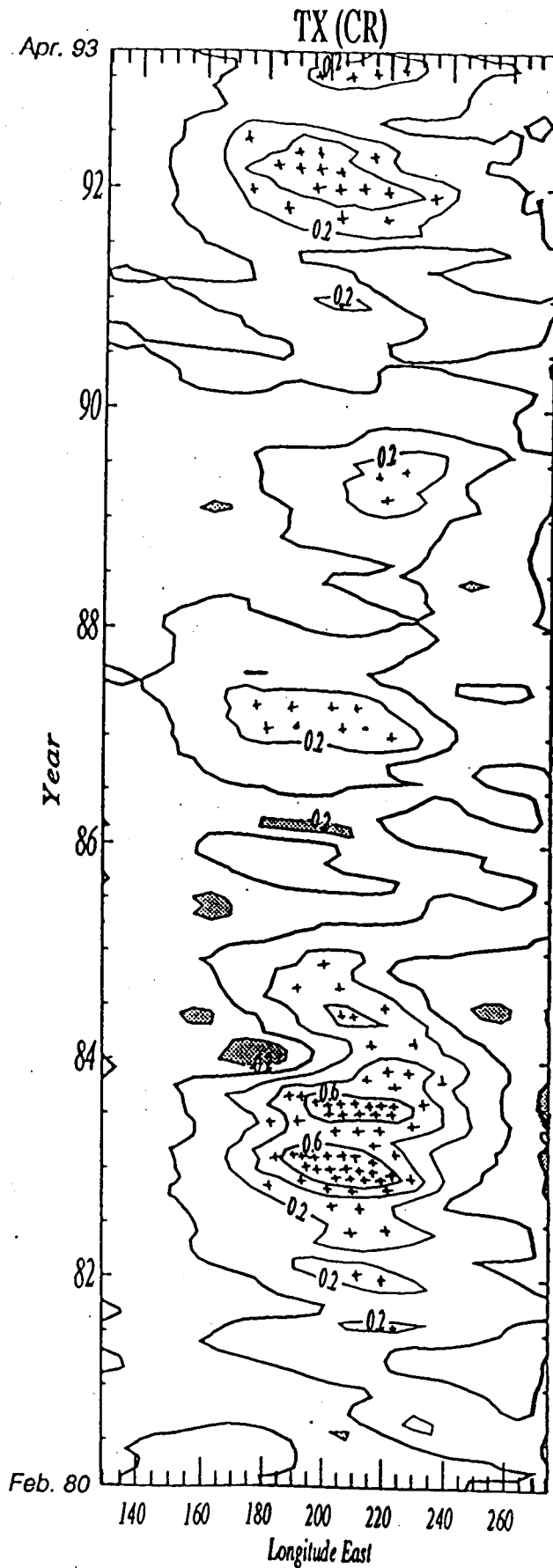


Fig 15

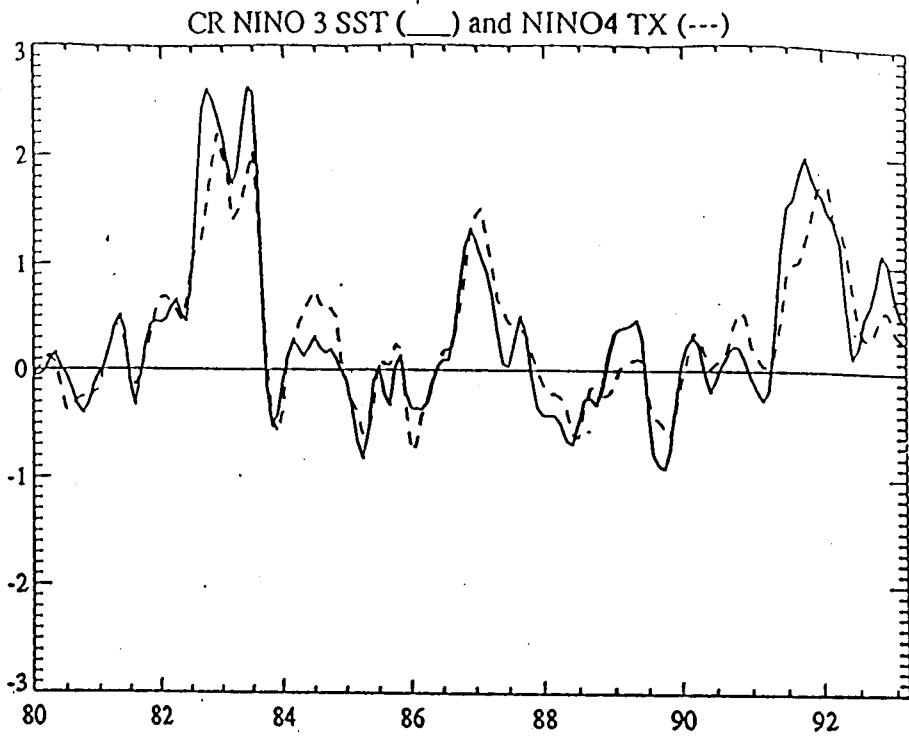


Fig. 16a

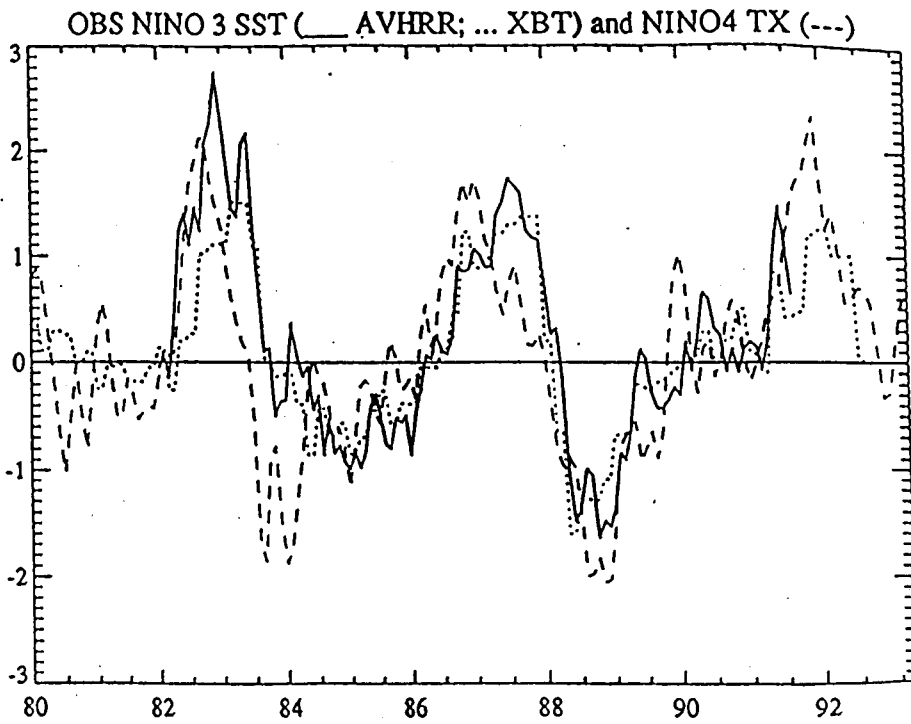


Fig. 16b

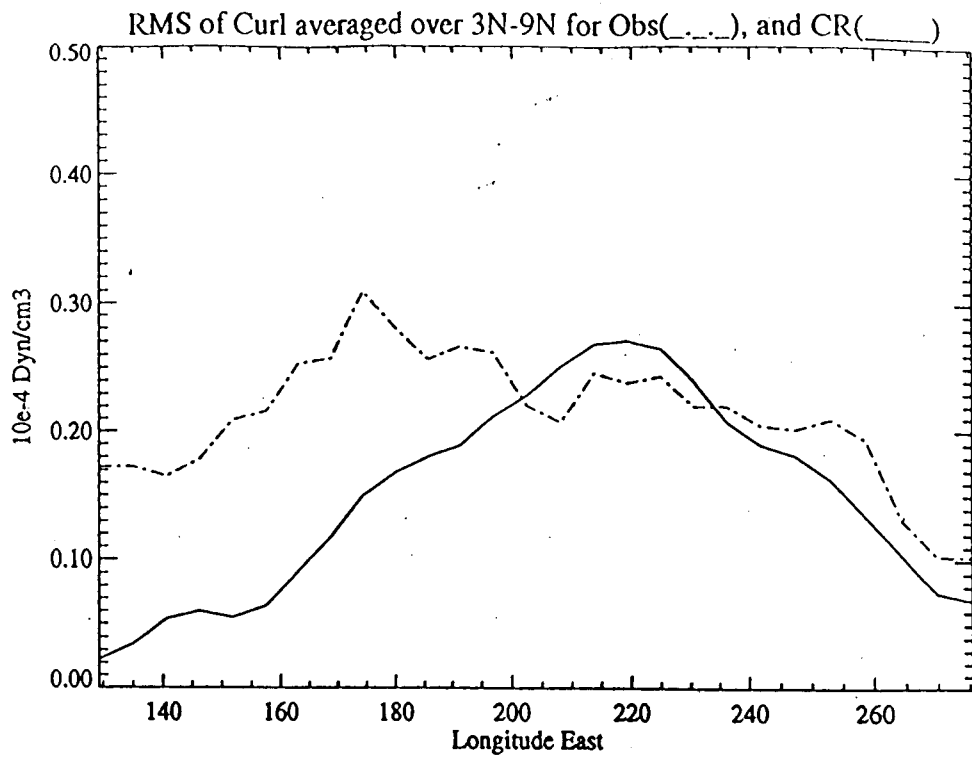


Fig. 17a

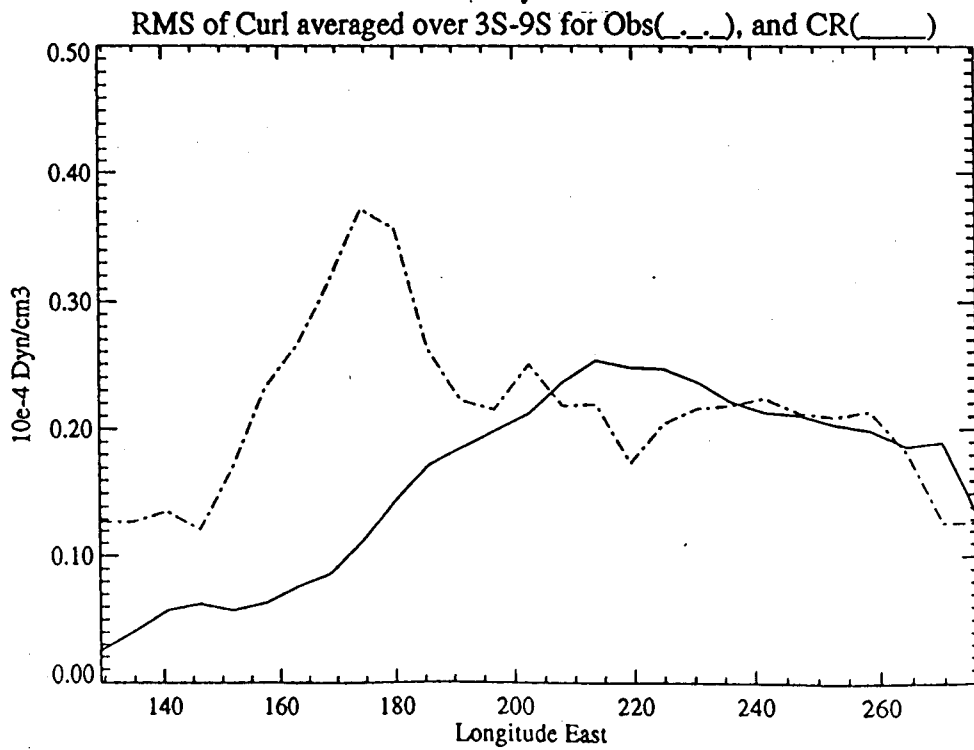
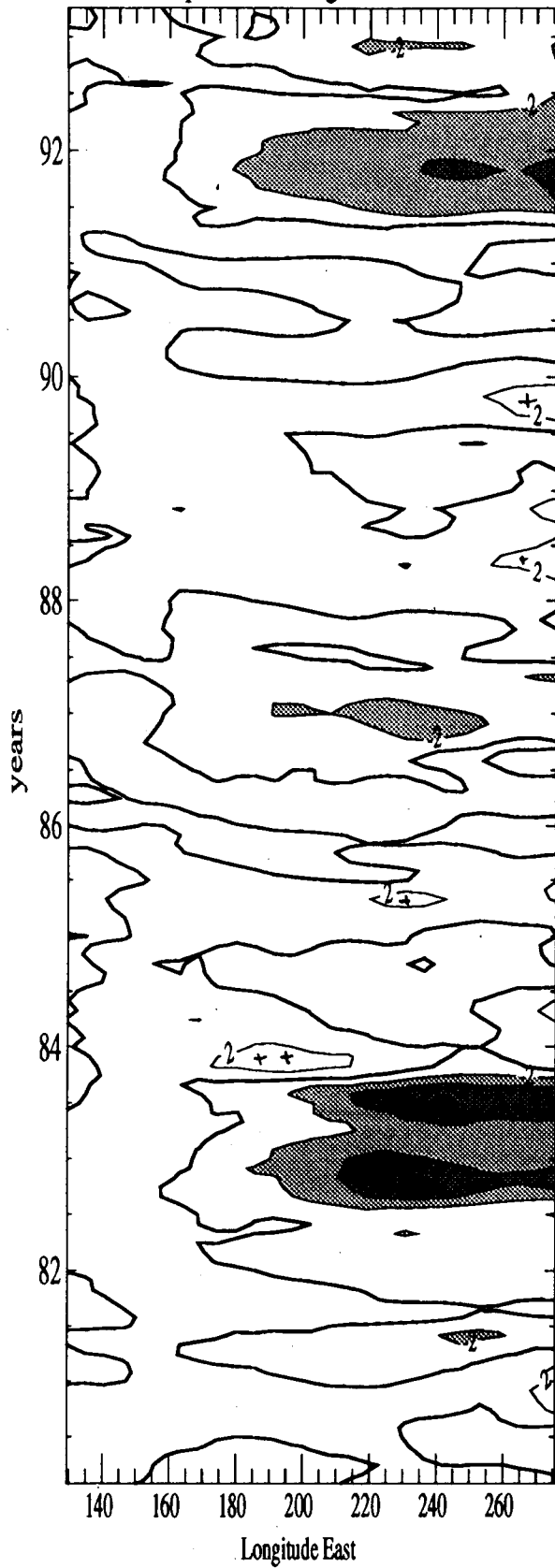


Fig. 17b

Atmospheric forcing term from CR



Convective forcing term (ISCCP)

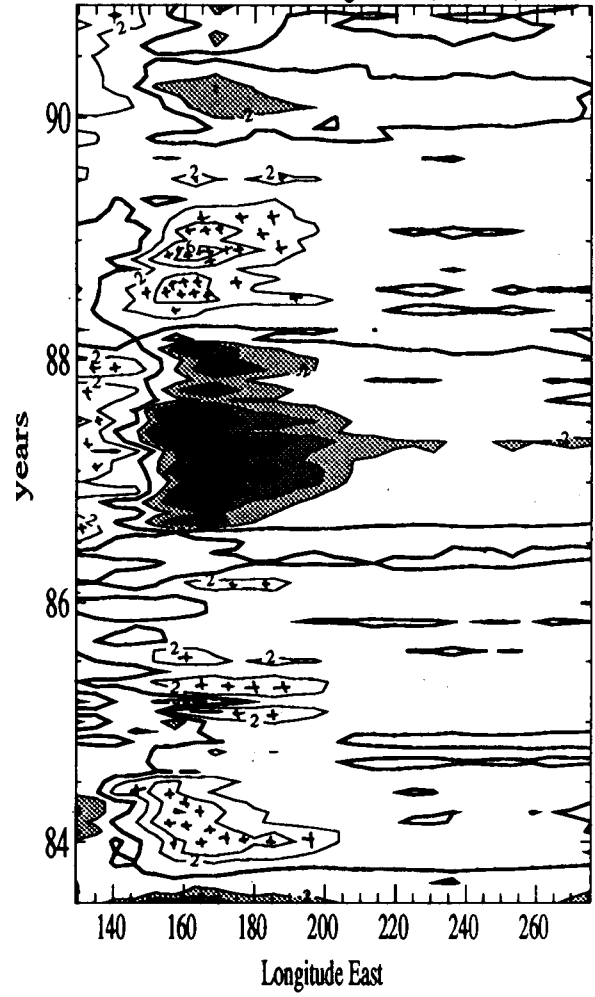


Fig 18ab

**Table 1a** : Correlation and RMS of sea level compared with Geosat (Apr. 85-Sept. 89)

Index	CORRELATION				RMS (cm)				RMSDIFF (cm)			
	NINOW	NINO4	NINO34	NINO3	NINOW	NINO4	NINO34	NINO3	NINOW	NINO4	NINO34	NINO3
GEOSAT	1	1	1	1	5.18	4.47	5.22	3.53	0	0	0	0
XBT	0.89	0.70	0.86	0.83	4.91	2.02	3.97	4.27	2.41	3.39	2.71	2.41
CR	0.77	0.37	0.80	0.79	6.88	3.05	4.55	5.78	4.36	4.37	3.17	3.68
O.BNDY0	0.84	0.33	0.72	0.67	6.57	2.95	3.90	4.74	3.58	4.46	3.62	3.52
O.FRIC	0.81	0.22	0.77	0.79	6.62	2.63	3.62	4.87	3.84	4.65	3.34	3.02

**Table 1b** : Correlation and RMS of sea level compared with XBT data (Feb. 80-Aug. 92)

Index	CORRELATION				RMS (cm)				RMSDIFF (cm)			
	NINOW	NINO4	NINO34	NINO3	NINOW	NINO4	NINO34	NINO3	NINOW	NINO4	NINO34	NINO3
XBT	1	1	1	1	4.48	3.86	4.12	4.13	0	0	0	0
CR	0.63	0.48	0.60	0.78	7.03	3.96	4.02	5.73	5.45	3.96	3.66	3.60
O.BNDY0	0.79	0.57	0.56	0.76	6.80	4.82	4.08	4.06	4.28	4.10	3.86	2.84
O.FRIC	0.68	0.48	0.60	0.81	6.34	3.62	3.32	4.91	4.64	3.80	3.42	2.86

**Table 2** : Correlation and RMS of SST (Apr. 85-Sept. 89).

Index	CORRELATION			RMS (°C)			RMSDIFF (°C)		
	NINO4	NINO34	NINO3	NINO4	NINO34	NINO3	NINO4	NINO34	NINO3
AVHRR	1	1	1	0.64	0.92	0.93	0	0	0
XBT	0.97	0.95	0.94	0.63	0.86	0.86	0.15	0.29	0.31
CR	0.79	0.65	0.56	0.34	0.46	0.52	0.43	0.71	0.77
O.BNDY0	0.92	0.88	0.86	0.45	0.62	0.67	0.29	0.47	0.49
O.FRIC	0.84	0.71	0.60	0.34	0.46	0.50	0.41	0.67	0.74

**Table 3 : Correlation and RMS of zonal current compared with Geosat.**

<i>Index</i>	CORRELATION			RMS (cm/s)			RMSDIFF (cm/s)		
	NINO4	NINO34	NINO3	NINO4	NINO34	NINO3	NINO4	NINO34	NINO3
GEOSAT	1	1	1	14.35	15.35	12.63	0	0	0
CR	0.59	0.56	0.43	9.93	10.09	8.94	11.72	12.56	11.89
O.BNDY0	0.70	0.58	0.54	15.43	13.68	12.13	11.52	13.19	11.91
O.FRIC	0.74	0.69	0.55	8.96	8.66	7.41	9.77	11.04	10.58

**Table 4a** : Correlation and RMS of zonal wind stress (Apr. 85-Sep. 89).

<i>Index</i>	CORRELATION		RMS (Dyn/cm <sup>2</sup> )		RMSDIFF (Dyn/cm <sup>2</sup> )	
	NINO4	NINO34	NINO4	NINO34	NINO4	NINO34
FSU	1.0	1.0	0.19	0.14	0.0	0.0
CR	0.67	0.45	0.10	0.09	0.15	0.13
O.BNDY0	0.67	0.60	0.14	0.13	0.14	0.12
O.FRIC	0.64	0.36	0.10	0.10	0.15	0.14

**Table 4b** : Correlation and RMS of meridional wind stress (Apr. 85-Sep. 89).

<i>Index</i>	CORRELATION		RMS (Dyn/cm <sup>2</sup> )		RMSDIFF (Dyn/cm <sup>2</sup> )	
	NINO4N	NINO34N	NINO4N	NINO34N	NINO4N	NINO34N
FSU	1.0	1.0	0.13	0.14	0.0	0.0
CR	0.24	0.29	0.03	0.04	0.13	0.14
O.BNDY0	0.33	0.60	0.03	0.04	0.12	0.13
O.FRIC	0.32	0.26	0.02	0.03	0.12	0.14

<i>Index</i>	CORRELATION		RMS (Dyn/cm <sup>2</sup> )		RMSDIFF (Dyn/cm <sup>2</sup> )	
	NINO4S	NINO34S	NINO4S	NINO34S	NINO4S	NINO34S
FSU	1.0	1.0	0.08	0.07	0.0	0.0
CR	0.38	0.32	0.03	0.03	0.07	0.06
O.BNDY0	0.54	0.27	0.05	0.04	0.07	0.07
O.FRIC	0.44	0.31	0.03	0.03	0.07	0.06